Short-range Forecasting Research

GLOBAL PRECIPITATION CLIMATOLOGY PROJECT ALGORITHM INTERCOMPARISON PROJECT - 2

REPORT No. 5

GPCP-AIP/2 - ATLAS: AVHRR DATA

by

G.L. Liberti

December 1992

Meteorological Office
London Road
Bracknell
Berkshire
RG12 2SZ
United Kingdom

GPCP-AIP/2 - ATLAS: AVHRR DATA.

*G.L.Liberti**
Meteorological Office,Bracknell, UK

10 th December 1992

Introduction

As part of the Global Precipitation Climatology Project - Algorithm Intercomparison Project - 2 (GPCP-AIP/2) (WMO, 1989) data from the Advanced Very High Resolution Radiometer (AVHRR) (Schwalb, 1978) on board of the NOAA series of polar orbiters (NOAA-10 and NOAA-11) were collected, for the period 1^{st} February to 9^{th} April 1991, for the orbits covering the area shown in Figure 1. The images were collected for satellite passes within the time intervals reported in Tab.1.
The AVHRR is a 4 (5 for the AVHRR-2 on board of NOAA-11) channel radiometer with the spectral response as reported in Tab.2.
Statistical analyses were carried out on the data set in order to:
- test the quality of the data;
- study the statistical properties of the data;
- help select interesting cases from the point of view of estimating precipitation;
- compare with similar analyses of data sets from other instruments during the GPCP-AIP/2 Campaign.
This report shows the results of these analyses. Preliminary results were published in Liberti (1991).
The data origin and preprocessing are described in Section 1.
Section 2 describes the analyses applied to the data set.
In Section 3 some comments on the data set are reported.

1 Data origin and Preprocessing

The UK Meteorological Office obtained imagery data from the NOAA series of polar orbiters (NOAA-10 and NOAA-11) in real-time using their dedicated satellite image processing system, Autosat-2 (Allam et al. 1990).
The operational nature of the Autosat-2 system imposed a number of limitations on the form of the imagery data. The absence of an internal archive of imagery implied that missed or corrupted data had to be obtained from external sources.
Hence, additional imagery data from University of Dundee were obtained to improve the availability of the imagery but they are not included in this analyses.
Apart from a very few seriously contaminated images, all the images produced by Autosat-2 have been analysed. Some more rigorous criteria discriminating low quality data can be suggested (see Section 3) but have not been applied at this stage, to give users maximum flexibility to process the data.

The imagery preprocessing (Navigation, Calibration, Rescaling) is described below.

1.1 Navigation

In general, Autosat-2 produces images on predefined areas in specified map projections, usually polar stereographic, using a nearest-neighbour method. However, for the AIP-2, AVHRR products were originally produced on an area which was incorrectly defined, and not quite a true rectangle on a standard

*EUMETSAT Research Fellow

polar stereographic projection. Knowing the exact definitions of both the old (incorrect) and new (correct) areas, post processing was carried out on all images to correct for this error. This is the cause of the bands containing "missing data" values which can be seen on the extreme east and west of the images. The AVHRR data, however, were also affected throughout the acquisition period by various problems with the Autosat-2 navigation software. These caused the accuracy of the navigation of many of the images to be inadequate for the experiment (especially during the early part of the period).

A corner correction has therefore been applied to the AVHRR images using visual inspection. The images were shifted linearly until the best fit was found between the coastline observed in the image and the nominal coastline associated with the area. This procedure was only possible, of course, when the coast was evident in the image. The header of each image carries information on whether this renavigation was possible, the magnitudes of the shifts applied and a flag indicating the image navigation quality (blank, corrupted etc).

The final products are in the form of digital imagery of 600 lines x 720 pixels. The pixel size is 2.5x2.5 km, whereas the original resolution was ranging approximately from 1.1x1.1 km at nadir to approximately 4.5x1.5 km at the end of the scan line. In the final product, information about the position of the original pixel in the scan line is lost.

1.2 Calibration

The raw radiometric data, consisting into 10-bits counts (0-1023), were calibrated into Albedo [%] for the channels 1 and 2 (in the following referred as Visible channels) and Brightness temperature [K] for the channels 3,4 and 5 (in the following referred as Infrared channels) according with the following schemes.

AVHRR visible channels ($i = 1$ or 2) counts were converted into Albedo using the following equation:

$$A = (\nu_i C_i + \delta_i) * \sec\phi \tag{1}$$

where:

A is Albedo [%] (see Section 3);

C_i is raw counts in AVHRR channel i;

ν_i, δ_i are calibration constants pertaining to each AVHRR instrument reported in Tab.3;

$\sec\phi$ is the secant of the solar zenith angle (computed for each pixel).

The conversion of AVHRR infrared channels ($i = 3,4$ or 5) into brightness temperature counts is a two step procedure..
Firstly the raw counts were converted into radiances as follows:

$$R_i = G_i C_i + I_i \tag{2}$$

R_i is the radiance of the scene for channel i [mW/(sr m^2 cm^{-1})];

G_i is the 'gain' and I_i is the 'intercept' for channel i derived from radiometric measurements of the internal black-body (the radiance of which is computed, using a sensor-weighted integral from temperatures values independently measured using 4 platinum resistance thermometers) and of space (assumed to have zero radiance).

C_i is the measured count.

New calibration parameters (G_i and I_i) were computed every 50 lines, averaging over 50 lines to obtain the internal blackbody radiance value and using the last 5 lines (of such a 50 lines block) for radiometric counts for both 'hot' and 'cold' points. These calibration parameters are applied to the next 50 lines.
Secondly, the temperature corresponding to this radiance was computed as follows. Temperature-radiance look-up tables were generated for each channel and each satellite, by calculating the integrated radiance (weighted by the appropriate channel's spectral response) for a set of scene temperatures at an interval of 0.1 K [150.1 to 350.0 K]. Temperatures corresponding to the set of radiances generated from the linear relationship with counts were subsequently determined by linear interpolation between appropriate look-up table entry values.
Finally, for channels 4 and 5, temperature corrections (functions of the channel and of the internal blackbody and scene temperature) were applied to account for the non-linear nature of the relationship between counts and radiance (Brown et al. 1985). These corrections were determined by interpolating linearly from the values supplied by NOAA-NESDIS (Appendix B, Lauritson et al. 1988) (see *Tab.4*).

During the GPCP-AIP/2 campaign, the non-linear correction for NOAA-10 was inadvertently applied to NOAA-11. Since the AVHRR on NOAA-10 did not have a channel 5, no correction was made for this channel for NOAA-11. The impact of this error is discussed in Section 3.

Once the product value (temperature or albedo) was determined for a particular pixel, a linear scaling was then applied to obtain a pixel value in the range 0→254 (corresponding to a temperature range of 198-308 K or albedo range of 0-100%). The digitization interval is 0.3937 Albedo % for CH1 and CH2 data and 0.433 K for CH3, CH4 and CH5 data.

2 Results Summary

Tab.5 summarises the amount of data used for the analyses.
Because of the dual nature of the information (emittance/reflectance) in the AVHRR Channel 3, data have been divided into 3 classes, and considered as independent channels, according to the time of the day:

- Night-time ($CH3_n$): time<6:00 or time>18:00;
- High solar zenith angle ($CH3_m$): 6:00≤time≤9:00 or 16:00≤time≤18:00
- Low solar zenith angle ($CH3_d$): 9:00<time<16:00

Fig.3.a shows the number of channel 3 images within each hour for each month during the GPCP-AIP/2 campaign. Also *Fig.3.b* shows the curve of the solar elevation angle $[90^o - \phi]$ computed for the first day of each month [February, March, April] for the approximate centre of the image ($47^oN - 0^oE$); the corresponding values of $\sec\phi$ are shown in *Fig.3.c*.

For each channel and each image, the following products have been produced:

- Number of pixels analysed [N];

- Minimum [min] and maximum [MAX] value;

- Mean:

$$\bar{x} = \frac{\sum_{i=1}^{N} x_i}{N}$$

- Standard Deviation:

$$s_2 = \sqrt{\frac{\sum_{i=1}^{N}(x_i - \bar{x})^2}{N-1}}$$

- Coefficient of Skewness:

$$s_3 = \frac{\sum_{i=1}^{N}(x_i - \bar{x})^3}{(N-1)\cdot s_2^3}$$

- Coefficient of Kurtosis:

$$s_4 = \frac{\sum_{i=1}^{N}(x_i - \bar{x})^4}{(N-1)\cdot s_2^4} - 3$$

- Frequency distribution for classes as specified in *Tab.6*;

Although the distributions are expected to be bi- or tri-modal and hence not normal, the coefficient of Skewness and Kurtosis were computed and reported as parameters contributing to the description of the distribution.
For each month the results are shown in form of summary panels (*Fig.4-24*)

Referring to *Fig.4-24*, each summary panel contains the following information:
FRAME A: Time series of the number of images available for each day;
FRAME B: Time series of the percentage of pixels of the full image containing useful data;
FRAME C: Time series of the frequency histogram where the contour lines correspond to [1] 1%, [2] 10%, [3] 25%, [4] 50% for the classes reported in *Tab.6*;
FRAME D: Time series of the coefficient of Kurtosis;
FRAME E: Time series of the coefficient of Skewness;
FRAME F: Time series of the Standard Deviation;
FRAME G: Time series of the mean, minimum and maximum values;
FRAME H: Cumulative histogram for the classes reported in *Table 6*;
FRAME I: Frequency distribution [%] of values for the coefficient of Kurtosis;
FRAME J: Frequency distribution [%] of values for the coefficient of Skewness;
FRAME K: Frequency distribution [%] of values for the Standard Deviation;
FRAME L: Frequency distribution [%] of values for mean (continuous line) minimum and maximum (dashed lines).
In the April panels *Fig.6,9,12,15,18,21,24*, the column of plots on the extreme right represents the same as panels H to L except for the whole period.
The axis limits, interval and unit of measurement are shown in *Table 7*.

For each time series of statistical parameters computed from the images, some basic statistics (minimum and maximum value, mean, Standard Deviation, Skewness and Kurtosis) have been also calculated. The results are shown in (*Table 8.a-g.*) for each month as well as for the whole period (ALL).

3 Discussion of problems

Because of limitations and problems with Autosat-2, only 80 % of the images potentially available during the GPCP-AIP/2 campaign have been analysed: serious gaps of data occurred especially in February, at the beginning of the campaign.

Also, due to the orbital characteristics of the NOAA polar satellites, the images analysed have different sizes and the data analysed within each image may cover different regions according to the relative position within the image. This has to be taken into account when analysing statistical properties of each single image. However the cumulative properties, taken over a month or over the whole period, should be representative of the whole area. For statistical purposes, it may be useful to produce daily statistics, rather than those for single images, in order to minimize the effects of different size and scene as well as diurnal cycles in the signal, this should not seriously affect the cloud-precipitation signal because of the large space and time scales of the weather systems of interest.

The original spatial resolution of the AVHRR data ranges from 1.1x1.1 Km at the nadir to 1.5x4.5 Km at the edges of the scan line. The GPCP-AIP/2 AVHRR images have a resolution of 2.5x2.5 km arising from a remapping based on a nearest neighbour method, resulting in a sampling approximately every 2 lines. In the scanning direction, approximately 87.5 % of the data have a resolution <2.5 km; this results in an under-sampling in the central part of the scan and in a repetition of values at the final edges of the scan. Because this information is lost in the final imagery product, caution is required in the use of

spatial pattern analysis (see for example Ebert, 1988 or Karlsson and Liljas, 1990).

The raw AVHRR radiometric data, as received from the NOAA polar satellites, are 10-bits counts proportional to the radiance measured by the radiometer. The final GPCP-AIP/2 imagery products are 8-bit albedo/brightness temperature values.
In general, when converting original 10-bits values into 8-bits ones over a similar range, a loss in accuracy of the final product is expected. For the Infrared channels, the original counts are "linearly" proportional to the radiance detected, but the final product values are instead linearly proportional to brightness temperature; the loss in accuracy is more complex than just the loss of two bits and is wavelength dependent.

Fig.25 shows the correspondence between digital count and brightness temperature for the original 10-bits counts compared with that for the GPCP-AIP/2 products, for channels 3 and 4 (channel 5 being similar to channel 4).
Because of the form of the Planck blackbody function, the colder end of the temperature scale of the products has a lower inherent resolution and therefore not all levels are expected to be occupied in the final arrangement. This is much more evident for channel 3. At low temperatures (200 K), the original data have a precision of only about 10 K (compared to approximately 0.8 K for channel 4). A detailed discussion on the radiometric precision at low temperatures can be found in Ebert and Holland (1992) and in Yamanouchi et al. (1987).
Fig.26 shows an example of T4 vs T3 scatterplot for all the images available for the day 19/03/91. Gaps of unpopulated levels in the lower end of distribution may be observed as a consequence of the effect discussed above (see for example scatterplot for 02:23 UT). However, this effect is not as clear as expected because of the use of several calibration curves ($\simeq 12$) within the same full-frame image (see Section 1.2). For the warmer end ($T3 > 280$ K), the original radiometric resolution is instead degraded.
An optimization of such a conversion may be obtained storing radiance values for the IR channels rather than brightness temperatures.

Whereas the upper limit of the original data is approximately 320 K, the GPCP-AIP/2 products have been restricted to 308 K. For Channel 4 and 5, the loss of information is negligible ($<$ 20% of the potentially available range, see Fig.25) especially regarding cloud and precipitation studies. In the case of channel 3, for such a upper boundary choice, circa 400 10-bit count levels (40 % of the original data range) are therefore represented by a single 8-bit count at the upper end. As a consequence, part of the quantitative information about the tops of bright clouds during daytime or sunglint over sea is therefore lost.
As an example, note the distribution of T3 values for daytime images (08:27, 13:15, 13:55, 16:36) in *Fig.26*. The values of T4 corresponding to the saturation of T3 ($T3 \geq 308K$) show that both surface and cloud surface can be responsible for this saturation.

Although noisier data are generally expected from channel 3, the occurrence of low quality data, appearing as bands (due to the calibration procedure, see Section 1.2) seems to be observed mostly for evening (ascending orbit) imagery. Such a disturbance may be due to the passage from illuminated to not-illuminated conditions as discussed by Steyn-Ross et. al. (1992). More detailed analyses are needed.

The non-linear temperature correction applied to NOAA-10 channel 4 and 5 was performed with blackbody temperature values different from the published ones (see Tab.4). Due to the final temperature resolution, the effect can be considered negligible.

During the GPCP-AIP/2 campaign, the non-linear corrections for NOAA-10 were inadvertently applied to NOAA-11. Since the AVHRR on NOAA-10 did not have a channel 5, no correction was made for this channel on NOAA-11.
In the absence of information about the temperature of the internal blackbody, only an average value for the corrections can be given together with possible extreme values.
Whereas the effect of such an error for the T4 value would be expected to be within 1 digitization interval (i.e. about 0.43 K) for most of the range (T4>225 K), for T5, it can be as much as 1 K at both ends of the range and therefore a colder and warmer values respectively for the minima and for the maxima are expected for the corrected images.
More significant is however the error associated with the difference, T4-T5. Such a difference has been

widely used for cloud studies (see Wu (1987), Parol et al. (1991), Prabhakara et. al (1988), Inoue (1987a), Olesen and Grassl (1985), Takano et al. (1992)), especially for the discrimination of optically thin clouds (for precipitation purposes considered as non-precipitating (Inoue (1987b)). The error can be as much as 2 K i.e. of the order of magnitude of the threshold generally applied. *Fig.27.C* shows a simulation of the error, obtained assuming T5=T4. Over thin cirrus clouds, however, the error is expected to be less because $T5 > T4 + 2.5$.
A direct consequence of the application of algorithms using such a difference to precipitation estimates (Karlsson 1990, Inoue 1987b) is expected to appear as an overestimation of precipitating areas.
Because the internal target temperature information is not available and because the corrections at different internal target temperature are smaller than the digitization interval, a correction obtained from averaging the errors is suggested and reported in *Tab.9*. Such a correction should be applied only to the NOAA-11 data (See *Tab.1*).
The effects of such error on the derived image T4-T5 have been studied, as an example, for two of the GPCP-AIP/2 selected cases: 91/03/08-02:46 and 91/03/26-02:44. For both cases the derived image T4-T5 has been produced using, uncorrected GPCP-AIP/2 data as well as using the correction reported in *Tab.9*.
Fig.28 shows scatterplots T4-T5 vs T4 for such images. It is evident that the effect of the correction is most significant at the colder end of the T4 scale, where most of the negative T4-T5 differences points disappear after the correction is applied.
Some statistics from T4-T5 images for the two cases are shown in *Fig.29*. Both the distribution (up to 15% difference in the population of some classes) and the statistics are different for the corrected images. The difference in the average value over the image is $\simeq 0.8$ K in both cases. Due to the limited range of the T4-T5 variable, such a difference is comparable with the size of the signal and therefore cannot be neglected.
Also, large areas of negative T4-T5 over the cold cloud top, which are very difficult to interpret from a physical point of view (see for example Prata (1989), Yamamouchi et al. (1987)) can be observed when using data from the GPCP-AIP/2 data set. *Fig.30* shows mask values (white: $T4 > T5$, black: $T4 < T5$) for two selected cases, using the original data and applying the correction (see below).

During the GPCP-AIP/2 calibration coefficients for the visible channels, different from the ones published by NOAA (Appendix B- Lauritson et al. 1988), were used in eq.1 (see *Tab.3*). The origin of these coefficients is unknown. The effects of their use have been investigated. *Fig.31* shows the percent difference ($D = 100. * (A_{Autosat2} - A_{NOAA})/A_{NOAA}$) between the albedo as computed for the GPCP-AIP/2 and the one obtained using the NOAA calibration coefficients for solar zenith angle values of: 88°, 80°, 70°, 60°, 50° and 40°.
Excluding the low sun elevation angles, whereas for NOAA-10, the difference (negative) can be considered to be negligible in both channels, for NOAA-11, differences of $\simeq 6\%$ and $\simeq 9\%$ have been computed respectively for channel 1 and channel 2.

An overestimation of precipitating areas is therefore expected from both the incorrect infrared and visible calibrations of the NOAA-11 data.

In the GPCP-AIP/2 data set, pixels with solar zenith angle ($\phi > 88^o \Rightarrow sec\phi = 28.7$) were classified as "missing data". Because of extreme physical conditions for such a low illumination angle (high anisotropy in surface reflection, strong atmospheric effects, etc.) as well as numerical problems due to high value of $sec\phi$ (for which one 10-bit count account for $\simeq 3\%$ Albedo, *Fig.2*, see also *Fig.31*) the choice of the threshold seems to be to high. The effect of such a choice can be easily observed in the time series of the statistics for channel 1 and channel 2. For example, panel G of *Fig.4-to-9* shows a consistent diurnal cycle of the value of the average with maxima for low illuminated images: the sharpness of the peaks decreases with time.
Also the values of the maximum, almost constantly 100 % for the month of February, decrease during the month to more realistic values. Similar effects can be observed in the distribution (panel H of *Fig.4-to-9*) of the values within the images.
From *Fig.2-3-31* it can be seen that choosing a threshold value $\phi > 80^o$ should avoid very extreme conditions, minimizing numerical effects, although still critical for some physical assumptions.
Therefore the images/pixels with very low sun elevations should be used cautiously.

No correction for the ellipticity of the earth's orbit has been applied in the computation of eq.1. The required intensity correction factor ranges from 1.029 (1 Feb.) to 0.997 (9 Apr.) accounting for a difference of 3% in the value used as solar constant. The consequence of the omission of this factor from GPCP-AIP/2 visible data set is a downward trend, during the campaign, of the albedo value.

According to Rao (1987), the definition of a visible product as obtained from eq.1 is not albedo, or even planetary albedo, but: "the ratio of the irradiance of an isotropic radiation field with radiance I (the measured filtered radiance) to the filtered solar radiance". Because of the high solar zenith angle ($\phi > 40°$) during the GPCP-AIP/2 campaign (*Fig.3.b*), and the anisotropic properties of clouds for such illumination conditions (Taylor and Stowe, 1984), the values obtained can only be considered to be relative.
If an absolute value is needed, for example to apply modelled results, it may be more convenient to convert the count into radiance, then into bidirectional reflectance. A detailed discussion on the conversion of AVHRR visible counts in to radiance and/or broadband albedo may be found in Saunders (1990), Price (1987) and Wydick et al. (1987).

A further limit to the quantitative use of AVHRR visible channels is given by the uncertainty in the calibration. The calibration information available derive from the pre-launch period; a change in the performance of the radiometer can be expected during the operational lifetime. A degradation of the characteristics of the visible channels has been observed in the past (Staylor, 1990, Holben et al. 1990). Due to the different lifetimes of the satellites used in the GPCP-AIP/2 the effect can be not only an uncorrected value of the measurement but can differ in entity depending upon the satellite.

Finally, in *Tab.10*, the list of GPCP-AIP/2 selected passes (i.e. the passes for which instantaneous precipitation estimation have been requested to the GPCP-AIP/2 participants) is reported. Also, in the frame B of *Fig.19,20,21*, the points relative to the selected passes have been circled.

*****

The author is grateful to Dr. J.Foot for his help in producing this report, to Mr J.S.Armstrong and for his help in editing it, to Mr.K.-G.Karlsson (SMHI) for his collaboration, and to R.Allam, G.Holpin, P.Jackson and D.Offiler for their technical assistance.

REFERENCES

Allam, R.J., P.Dibben, G.Holpin, F.Smith and A.P.Standley, 1990. The use of satellite imagery products for operational meteorology. Proceedings of the 5th Conference on satellite meteorology and oceanography, held in London, 3rd-7th September 1990, 401-403. Published by the American Meteorological Society.

Brown O.B., J.W.Brown and R.H.Evans, 1985. Calibration of Advanced Very High Resolution Radiometer Infrared Observations. J. Geophys. Res. Vol 90 No C6 pp 11667-11677.

d'Entremont, R.P. and T.J.Kleespies, 1988. Possible measurements error in calibrated AVHRR data. Environmental Research Papers, 1001. AFGL-TR-88-0105, US Air Force Geophysics Laboratory.

Ebert, E.E. and G.J.Holland, 1992. Observation of record cloud-top temperatures in tropical cyclone Hilda (1990). Monthly Wea. Rew., 120, 2240-2251.

Ebert, E.E., 1988: Classification and analysis of surface and clouds at high latitudes from AVHRR multispectral satellite data. Scientific Report n.8, Feb.1988. Dept. of Met. Un. of Wisconsin - Madison. pp. 184

Inoue, T., 1987a: Cloud type classification with NOAA-7 split-window measurements. J.Geophys.Res. Vol 92 No D4, 3991-4000.

Inoue, T., 1987b: An instantaneous delineation of convective rainfall areas using split-window data of NOAA-7 AVHRR. J. Met. Soc. of Japan, Vol 65 No 3, 469-481.

Karlsson, K.G. and E.Liljas, 1990: The SMHI model for cloud and precipitation analysis from multispectral AVHRR data. PROMIS-Report 10, SMHI.

Kidwell,K.B., 1985. NOAA polar orbiter data users guide. NOAA/NESDIS.

Lauritson,L., G.L.Nelson and F.W.Porto, 1979. Data extraction and calibration of TIROS-N/NOAA radiometers NOAA Technical Memorandum NESS 107

Liberti, G.L., 1991. GPCP-AIP/2 properties of the AVHRR data. Preliminary results. Proceeding of the 5th AVHRR Data Users' Meeting. Tromso, Norway, 24-28 June 1991. EUM P 09, 235-240.

Olesen, F.S. and H.Grassl, 1985: Cloud detection and classification over oceans at night with NOAA-7. Int.J.Rem.Sensing. vol.6. no.8. 1435-1444.

Parol, F., J.C.Buriez, G.Brogniez and Y.Fouquart, 1991: Information Content of AVHRR Channels 4 and 5 with respect to the effective radius of cirrus cloud particles. J. of Clim. and Appl. Meteor. vol.30, no.7, 973-984.

Prabhakara, C., R.S. Fraser, G.Dalu, M.C. Wu, R.J. Curran and T.Styles, 1988. Thin cirrus clouds: Seasonal distribution over Oceans deduced from Nimbus-4 IRIS. J. of Appl. Meteor. vol.27, no.4, 379-399.

Prata A.J., 1989. Observation of volcanic ash clouds in the 10-12 μm window using AVHRR/2 data. Int.J.Rem.Sensing, 10, nos. 4-5, 751-761.

Rao, C.R.N., 1987. Prelaunch Calibration of channels 1 and 2 of the AVHRR. NOAA Technical Report NESDIS 36. pp.iii+62

Saunders, R.W., 1990. The determination of broad band surface albedo from AVHRR visible and near-infrared radiances. Int.J.Rem.Sensing, 11, no.1, 49-67.

Holben, B.N., Y.J.Kaufman and J.D.Kendall, 1990. NOAA-11 AVHRR visible and near-IR inflight calibration. Int.J.Rem.Sensing, 11, no.8, 1511-1519.

Price, J.C., 1987. Calibration of satellite radiometers and the comparison of vegetation indexes. Remote Sensing of the Environment. 24, 15-27.

Schwalb, A., 1978. The TIROS-N/NOAA A-G Satellite series. NOAA Tech. Memorandum NESS 95. pp. 72.

Steyn-Ross, D.A., M.L.Steyn-Ross and S.Clift, 1992. Radiance calibration for AVHRR infrared channels. J. Geophys. Res. Vol 97, No.C5, 5551-5568.

Takano Y., K.N.Liou and P.Minnis, 1992. The effect of small ice crystals on cirrus infrared radiative properties. J. of Atm. Sc. 49, no.16, 1487-1493.

Taylor, V.R. and L.L.Stowe, 1984. Atlas of reflectance patterns for uniform earth and cloud surfaces (NIMBUS-7 ERB-61 Days). NOAA Technical Report NESDIS 10. pp.iii+66+App.22.3.

Weinreb, M.P., G.Hamilton, S.Brown and R.J.Koczor, 1990. Nonlinearity Corrections in calibration of AVHRR infrared channels. J. Geophys. Res. Vol 95, No.C5, 7381-7388.

W.M.O./T.D., 1989. The Global Precipitation Climatology Project. Report of the 4^{th} session of the international working group on data management. WMO/TD No. 356. Bristol, U.K., 26-28 July 1989.

Wu, M.C., 1987: A method for remote sensing the emissivity, fractional cloud cover and cloud top temperature of high-level, thin clouds. J. of Appl. Meteor. vol.26, no.2, 225-233.

Wydick, J.E., P.A.Davis and A.Gruber, 1987. Estimation of broadband planetary albedo from operational narrowband satellite measurements. NOAA Technical Report NESDIS 27. pp.iii+32.

Yamanouchi, T., K.Suzuki and S.Kawaguchi, 1987: Detection of clouds in Antarctica from Infrared multispectral data of AVHRR. J. Met. Soc. of Japan, Vol.65, No.6, 949-961.

TABLES

1. GPCP-AIP/2 time [UT] passes intervals.

	NOAA-10	NOAA-11
Decending	6:40-10:00	01:40-05:00
Ascending	16:40-20:00	11:40-15:00

2. Bandlimits (μm) for the AVHRR(-2) channels.

	NOAA-10	NOAA-11
CH1	0.58-0.68	0.58-0.68
CH2	0.725-1.1	0.725-1.1
CH3	3.55-3.93	3.55-3.93
CH4	10.3-11.3	10.5-11.5
CH5		11.5-12.5

3. Calibration coefficient for NOAA-10 and NOAA-11 channel 1 and 2 used in Autosat-2 for the GPCP-AIP/2 data set. In parentheses are shown the values from Appendix B Lauritson et. al. (1988).

	CH1		*CH2*	
	ν_1 [%/10-bit count]	δ_1 [%]	ν_2 [%/10-bit count]	δ_2 [%]
NOAA-10	0.10589 *(0.10588)*	-3.7261 *(-3.5279)*	0.10579 *(0.10607)*	-3.5692 *(-3.4767)*
NOAA-11	0.09500 *(0.0906)*	-3.7800 *(-3.730)*	0.09000 *(0.0827)*	-3.6000 *(-3.390)*

4. Non-linear corrections (from Weinreb et al.,1990) for NOAA-10 and NOAA-11 channel 4 and 5 [K]. Tt [K] is the brightness temperature as measured by each single channel. Tb [K] is the temperature of the internal calibration blackbody (in parentheses are shown the values used by Autosat-2).

	NOAA10-CH4			*NOAA11-CH4*			*NOAA11-CH5*		
Tb → Tt ↓	281.85 (283.15)	286.95 (288.15)	292.25 (293.15)	282.35	287.35	292.15	282.35	287.05	292.15
205	-2.47	-2.88	-3.27	-1.54	-1.76	-1.98	-1.15	-1.27	-1.23
215	-2.58	-2.65	-2.80	-1.82	-2.02	-2.20	-1.12	-1.24	-1.16
225	-2.22	-2.51	-2.53	-1.90	-2.14	-2.36	-0.94	-1.06	-1.16
235	-1.79	-2.20	-2.53	-1.87	-2.10	-2.28	-0.84	-1.02	-1.00
245	-1.74	-2.09	-2.26	-1.70	-1.96	-2.22	-0.72	-0.90	-0.92
255	-1.33	-1.49	-1.77	-1.41	-1.72	-2.03	-0.60	-0.77	-0.78
265	-0.76	-0.93	-1.37	-1.06	-1.37	-1.66	-0.37	-0.51	-0.60
275	-0.46	-0.53	-1.08	-0.45	-0.79	-1.15	-0.19	-0.34	-0.47
285	0.20	-0.15	-0.38	0.24	-0.21	-0.67	0.07	-0.07	-0.23
295	1.12	0.57	0.12	1.05	0.68	0.22	0.43	0.28	0.09
305	1.88	1.34	1.11	2.23	1.73	1.32	0.85	0.64	0.47
310	2.40	1.76	1.54	2.85	2.33	1.91	1.05	0.84	0.70
315	2.93	2.19	1.97	3.50	2.98	2.55	1.23	1.03	0.89
320	3.50	2.83	2.54	4.29	3.71	3.25	1.43	1.26	1.12

5. DATA STATISTICS:

(A) number of images analysed;
(B) % of expected number of images (assuming: 2 for $CH3_d$ and $CH3_n$, 4 for CH1, CH2, $CH3_m$ and CH5 and 8 for CH4 and CH3);
(C) number of pixels analysed;
(D) % of pixels analysed respect to the full frame for the images analysed.

	Period	A	B	C	D
C	Feb	70	62.5	20507555	67.8
H	Mar	113	91.1	34585564	70.8
1	Apr	32	88.9	9953679	72.0
	All	215	79.0	65046798	70.0
C	Feb	72	64.3	21009752	67.5
H	Mar	113	91.1	34587486	70.9
2	Apr	32	88.9	9953679	72.0
	All	217	79.8	65550917	69.9
C	Feb	37	66.1	12295088	76.9
H	Mar	56	90.3	18054497	74.6
3	Apr	16	88.9	5051425	73.1
d	All	109	80.1	35401010	75.2
C	Feb	40	71.4	12561279	72.7
H	Mar	61	98.4	19919612	75.6
3	Apr	19	100.0	6216468	75.7
n	All	120	82.2	38697359	74.6
C	Feb	67	59.8	21239320	73.4
H	Mar	107	86.3	33545373	72.6
3	Apr	30	83.3	9362720	72.2
m	All	204	75.0	64147413	72.8
C	Feb	144	64.3	46095687	74.1
H	Mar	224	90.3	71519482	73.9
3	Apr	65	90.3	20630613	73.5
	All	433	79.6	138245782	73.9
C	Feb	144	64.4	46102642	74.1
H	Mar	226	91.1	72057599	73.8
4	Apr	66	91.7	20948768	73.5
	All	436	80.1	139109009	73.9
C	Feb	71	63.4	23264782	75.9
H	Mar	111	89.5	36220824	75.5
5	Apr	34	94.2	10976463	74.7
	All	216	79.4	70462069	75.5

6. HISTOGRAM CLASSES:

class	CH1,CH2	CH3,CH4,CH5
1	$0 \leq A < 5$	$198 \leq T < 200$
2	$5 \leq A < 10$	$200 \leq T < 205$
3	$10 \leq A < 15$	$205 \leq T < 210$
4	$15 \leq A < 20$	$210 \leq T < 215$
5	$20 \leq A < 25$	$215 \leq T < 220$
6	$25 \leq A < 30$	$220 \leq T < 225$
7	$30 \leq A < 35$	$225 \leq T < 230$
8	$35 \leq A < 40$	$230 \leq T < 235$
9	$40 \leq A < 45$	$235 \leq T < 240$
10	$45 \leq A < 50$	$240 \leq T < 245$
11	$50 \leq A < 55$	$245 \leq T < 250$
12	$55 \leq A < 60$	$250 \leq T < 255$
13	$60 \leq A < 65$	$255 \leq T < 260$
14	$65 \leq A < 70$	$260 \leq T < 265$
15	$70 \leq A < 75$	$265 \leq T < 270$
16	$75 \leq A < 80$	$270 \leq T < 275$
17	$80 \leq A < 85$	$275 \leq T < 280$
18	$85 \leq A < 90$	$280 \leq T < 285$
19	$90 \leq A < 95$	$285 \leq T < 290$
20	$95 \leq A \leq 100$	$290 \leq T < 295$
21		$295 \leq T < 300$
22		$300 \leq T < 305$
23		$305 \geq T \leq 308$

7. PLOT SCALE AND MARKS:

FR: Reference frame;
Xm: Minimum value for the X-axis;
XM: Maximum value for the X-axis;
DX: Tick mark distance for the X-axis;
UX: Unit for the X-axis;
Ym: Minimum value for the Y-axis;
YM: Maximum value for the Y-axis;
DY: Tick mark distance for the Y-axis;
UY: Unit for the Y-axis;

AVHRR CH1,CH2 [Fig.2-7]

FR	Xm	XM	DX	UX	Ym	YM	DY	UY
A	1	*	1	DAY	0	9	1	IMAGES
B	1	*	1	DAY	10	101	10	PIXELS % OF THE FULL FRAME
C	1	*	1	DAY	0	10	10	ALBEDO %
D	1	*	1	DAY	-2	6	1	ALBEDO %
E	1	*	1	DAY	-2.5	1	0.5	ALBEDO %
F	1	*	1	DAY	0.0	30	5.0	ALBEDO %
G	1	*	1	DAY	0	100	10	ALBEDO %
H	0	40	5	% of total	0	100	10	ALBEDO %
I	0	30	5	% of total	-2	6	1	ALBEDO %
J	0	30	5	% of total	-2.5	1	0.5	ALBEDO %
K	0	30	5	% of total	0.0	30	5.0	ALBEDO %
L	0	30	5	% of total	0	100	10	ALBEDO %

AVHRR CH3,CH4,CH5 [Fig. 8-22]

FR	Xm	XM	DX	UX	Ym	YM	DY	UY
A	1	*	1	DAY	0	9	1	IMAGES
B	1	*	1	DAY	10	101	5	PIXELS % OF THE FULL FRAME
C	1	*	1	DAY	198	308	10	K
D	1	*	1	DAY	-2	6	1	K
E	1	*	1	DAY	-2.5	1	0.5	K
F	1	*	1	DAY	0.0	30	5.0	K
G	1	*	1	DAY	198	308	10	K
H	0	40	5	% of total	198	308	10	K
I	0	30	5	% of total	-2	6	1	K
J	0	30	5	% of total	-2.5	1	0.5	K
K	0	30	5	% of total	0.0	30	5.0	K
L	0	30	5	% of total	198	308	10	K

8. STATISTIC OF THE STATISTICS

A	*AVHRR-CH1*						
	Variable	Statistics of the variable					
		AV	S_2	S_3	S_4	min	MAX
F	AV [%]	42.71	17.29	1.08	0.22	18.09	89.06
E	min [%]	3.68	4.13	1.58	2.39	0.00	17.72
B	MAX [%]	99.43	2.02	-3.55	11.56	90.16	100.00
	S_2 [%]	21.58	4.88	0.72	-0.38	13.69	35.60
	S_3	0.18	0.80	0.32	1.72	-2.06	3.00
	S_4	-0.19	1.64	3.27	13.03	-1.39	8.79
M	AV [%]	42.60	14.10	0.91	0.62	17.24	85.87
A	min [%]	4.06	3.21	1.74	4.95	0.00	19.29
R	MAX [%]	96.51	7.29	-2.20	3.94	69.29	100.00
	S_2 [%]	21.03	3.74	0.82	0.59	14.34	32.86
	S_3	0.12	0.59	0.08	-0.10	-1.55	1.59
	S_4	-0.60	0.76	1.32	1.57	-1.71	2.25
A	AV [%]	35.33	10.35	1.04	0.27	22.34	62.17
P	min [%]	3.49	1.79	0.14	0.05	0.00	7.48
R	MAX [%]	95.73	8.01	-1.59	0.95	73.62	100.00
	S_2 [%]	20.58	2.17	0.14	0.26	15.31	25.97
	S_3	0.37	0.38	0.09	-0.85	-0.36	1.17
	S_4	-0.83	0.50	0.95	1.27	-1.67	0.68
A	AV [%]	41.55	14.93	1.10	0.79	17.24	89.06
L	min [%]	3.85	3.37	1.72	4.34	0.00	19.29
L	MAX [%]	97.34	6.37	-2.62	6.21	69.29	100.00
	S_2 [%]	21.14	3.97	0.89	0.63	13.69	35.60
	S_3	0.18	0.64	0.17	1.73	-2.06	3.00
	S_4	-0.50	1.12	4.02	25.14	-1.71	8.79

B	*AVHRR-CH2*						
	Variable	Statistics of the variable					
		AV	S_2	S_3	S_4	min	MAX
F	AV [%]	40.92	16.75	1.18	0.42	18.64	86.90
E	min [%]	2.12	2.89	2.15	4.33	0.00	12.60
B	MAX [%]	98.59	3.43	-2.28	3.73	87.01	100.00
	S_2 [%]	21.24	5.29	0.66	-0.77	13.03	34.84
	S_3	0.16	0.77	0.56	2.14	-1.96	3.05
	S_4	-0.18	1.60	3.62	16.69	-1.36	9.37
M	AV [%]	40.12	12.94	1.03	0.86	18.82	81.06
A	min [%]	2.60	2.82	2.67	9.46	0.00	18.11
R	MAX [%]	94.85	9.42	-1.75	1.95	63.39	100.00
	S_2 [%]	19.70	4.19	0.77	0.46	12.22	32.19
	S_3	0.12	0.54	0.03	-0.48	-1.25	1.29
	S_4	-0.49	0.73	1.08	0.68	-1.59	1.70
A	AV [%]	33.62	9.03	1.03	0.35	22.75	57.27
P	min [%]	1.97	1.30	0.51	-0.47	0.00	4.72
R	MAX [%]	93.18	10.68	-1.19	-0.21	66.54	100.00
	S_2 [%]	18.60	2.01	0.34	0.40	14.19	24.13
	S_3	0.28	0.36	0.12	-0.95	-0.33	1.07
	S_4	-0.65	0.60	1.28	1.18	-1.44	1.06
A	AV [%]	39.42	14.03	1.25	1.22	18.64	86.90
L	min [%]	2.35	2.68	2.56	8.56	0.00	18.11
L	MAX [%]	95.85	8.39	-2.08	3.43	63.39	100.00
	S_2 [%]	20.05	4.44	0.95	0.44	12.22	34.84
	S_3	0.16	0.61	0.36	2.25	-1.96	3.05
	S_4	-0.41	1.10	4.30	30.45	-1.59	9.37

C	*AVHRR-CH3$_d$*						
	Variable	Statistics of the variable					
		AV	S_2	S_3	S_4	min	MAX
F	AV [K]	282.99	3.50	0.08	-0.45	275.80	291.22
E	min [K]	243.17	15.54	-1.93	3.12	198.00	259.93
B	MAX [K]	307.86	0.67	-5.04	24.76	304.10	308.00
	S_2 [K]	10.73	1.69	-0.38	-0.57	7.34	14.02
	S_3	-0.18	0.39	0.18	0.32	-1.13	0.80
	S_4	-0.23	1.04	2.77	8.25	-1.17	4.14
M	AV [K]	285.81	5.19	0.10	-0.36	274.51	298.37
A	min [K]	248.62	11.68	-2.75	10.16	198.00	265.56
R	MAX [K]	308.00	0.00	0.00	0.00	308.00	308.00
	S_2 [K]	10.81	1.64	0.41	0.36	7.34	15.63
	S_3	-0.19	0.46	0.11	-0.82	-0.96	0.83
	S_4	-0.37	0.64	0.84	0.60	-1.44	1.59
A	AV [K]	288.42	4.90	-0.03	-1.40	279.67	295.22
P	min [K]	251.48	6.74	0.39	-0.20	241.74	266.86
R	MAX [K]	308.00	0.00	0.00	0.00	308.00	308.00
	S_2 [K]	10.91	1.88	0.29	-1.23	8.24	14.54
	S_3	-0.37	0.18	0.53	-0.81	-0.61	0.01
	S_4	-0.51	0.46	0.14	-1.34	-1.20	0.24
A	AV [K]	285.23	4.95	0.30	-0.33	274.51	298.37
L	min [K]	247.19	12.87	-2.45	7.23	198.00	266.86
L	MAX [K]	307.95	0.39	-9.04	83.74	304.10	308.00
	S_2 [K]	10.80	1.68	0.13	-0.17	7.34	15.63
	S_3	-0.21	0.41	0.28	-0.23	-1.13	0.83
	S_4	-0.34	0.78	2.64	11.16	-1.44	4.14

D	*AVHRR-CH3$_n$*						
	Variable	Statistics of the variable					
		AV	S_2	S_3	S_4	min	MAX
F	AV [K]	262.16	5.09	0.36	-0.77	253.56	271.69
E	min [K]	204.52	12.07	1.82	2.42	198.00	246.50
B	MAX [K]	295.92	9.74	-0.14	-1.36	279.85	308.00
	S_2 [K]	10.59	2.04	-0.68	0.79	4.14	14.17
	S_3	-0.61	0.81	-0.77	0.41	-3.02	0.74
	S_4	1.49	2.49	2.14	5.26	-0.85	11.65
M	AV [K]	261.55	7.21	0.03	-0.27	243.40	278.29
A	min [K]	204.91	14.22	1.87	2.02	198.00	248.24
R	MAX [K]	294.78	9.47	-0.03	-1.39	280.72	308.00
	S_2 [K]	13.28	4.26	0.30	-0.27	5.90	25.49
	S_3	-0.79	0.46	-0.11	-0.07	-2.00	0.38
	S_4	0.65	1.68	2.28	7.36	-1.19	8.67
A	AV [K]	266.51	5.67	-1.50	2.24	249.49	273.93
P	min [K]	208.37	12.92	0.89	-0.16	198.00	241.31
R	MAX [K]	297.79	9.35	-0.44	-1.28	281.15	308.00
	S_2 [K]	11.27	2.55	0.22	-1.17	7.49	16.24
	S_3	-0.86	0.41	0.56	1.01	-1.56	0.25
	S_4	0.42	0.85	0.46	-0.60	-0.99	2.27
A	AV [K]	262.54	6.53	-0.14	-0.26	243.40	278.29
L	min [K]	205.33	13.29	1.72	1.82	198.00	248.24
L	MAX [K]	295.64	9.52	-0.13	-1.36	279.85	308.00
	S_2 [K]	12.06	3.62	0.74	0.84	4.14	25.49
	S_3	-0.74	0.60	-0.34	1.09	-3.02	0.74
	S_3	0.89	1.94	2.59	9.16	-1.19	11.65

E	*AVHRR-CH3$_m$*						
	Variable	Statistics of the variable					
		AV	S_2	S_3	S_4	min	MAX
F	AV [K]	271.18	13.07	0.49	-0.56	247.97	300.36
E	min [K]	217.58	20.97	0.58	-0.96	198.00	265.56
B	MAX [K]	303.18	8.24	-1.49	0.77	281.15	308.00
	S_2 [K]	11.34	2.52	0.55	0.18	7.33	19.02
	S_3	-0.51	0.62	-0.49	-0.01	-2.35	0.63
	S_4	0.96	2.08	2.92	11.87	-1.34	12.28
M	AV [K]	276.84	12.95	0.12	-0.75	248.35	303.84
A	min [K]	226.33	23.15	0.07	-1.22	198.00	278.12
R	MAX [K]	304.96	6.90	-2.27	3.82	282.02	308.00
	S_2 [K]	12.58	4.16	1.44	2.91	6.34	29.14
	S_3	-0.43	0.63	-0.20	0.22	-2.24	1.15
	S_4	0.24	1.32	1.91	5.00	-1.46	6.59
A	AV [K]	282.04	10.44	0.17	-0.45	261.66	303.88
P	min [K]	231.75	23.65	-0.34	-1.23	198.00	270.76
R	MAX [K]	306.83	4.66	-4.50	19.49	283.31	308.00
	S_2 [K]	11.17	2.77	0.09	-0.82	6.68	16.91
	S_3	-0.50	0.52	-0.31	-0.89	-1.56	0.33
	S_4	0.34	1.19	0.80	-0.26	-1.59	3.20
A	AV [K]	275.75	13.11	0.16	-0.74	247.97	303.88
L	min [K]	224.25	22.98	0.18	-1.26	198.00	278.12
L	MAX [K]	304.65	7.18	-2.11	3.09	281.15	308.00
	S_2 [K]	11.97	3.55	1.51	4.16	6.34	29.14
	S_3	-0.47	0.61	-0.30	0.16	-2.35	1.15
	S_4	0.49	1.62	2.87	14.31	-1.59	12.28

F	*AVHRR-CH4*						
	Variable	Statistics of the variable					
		AV	S_2	S_3	S_4	min	MAX
F	AV [K]	262.04	5.67	-1.17	4.74	231.55	274.32
E	min [K]	218.39	7.21	-0.40	1.10	198.00	234.38
B	MAX [K]	286.13	7.18	1.88	3.21	270.76	308.00
	S_2 [K]	11.97	2.43	0.18	0.05	6.26	19.36
	S_3	-0.72	0.61	-0.42	1.76	-3.07	1.58
	S_4	0.59	1.59	2.70	10.78	-1.30	10.31
M	AV [K]	259.81	9.54	-0.31	-0.58	234.53	279.13
A	min [K]	213.51	7.14	0.43	0.80	198.00	240.01
R	MAX [K]	286.53	6.10	1.72	2.90	275.52	308.00
	S_2 [K]	15.97	5.05	0.38	0.05	4.16	31.31
	S_3	-0.71	0.66	-0.73	3.54	-4.45	1.09
	S_4	0.28	2.48	6.86	72.29	-1.85	28.49
A	AV [K]	265.87	6.43	-1.01	0.94	245.44	276.10
P	min [K]	217.17	8.81	-0.77	0.19	198.00	235.68
R	MAX [K]	290.62	8.67	0.85	-0.62	279.42	308.00
	S_2 [K]	13.84	3.80	0.38	-0.26	6.90	25.25
	S_3	-0.83	0.48	0.17	0.21	-2.06	0.53
	S_4	0.35	1.40	1.21	1.34	-1.66	4.85
A	AV [K]	261.47	8.26	-0.66	0.36	231.55	279.13
L	min [K]	215.68	7.76	-0.05	0.19	198.00	240.01
L	MAX [K]	287.02	7.06	1.62	2.10	270.76	308.00
	S_2 [K]	14.33	4.53	0.81	0.77	4.16	31.31
	S_3	-0.73	0.62	-0.54	2.93	-4.45	1.58
	S_4	0.39	2.08	6.41	76.47	-1.85	28.49

G	*AVHRR-CH5*						
	Variable	Statistics of the variable					
		AV	S_2	S_3	S_4	min	MAX
F	AV [K]	262.41	4.92	-0.21	0.86	245.36	273.30
E	min [K]	218.62	6.47	-0.35	1.67	198.00	235.24
B	MAX [K]	285.57	5.86	2.03	4.41	278.12	308.00
	S_2 [K]	12.25	2.37	0.33	0.24	6.44	19.22
	S_3	-0.76	0.58	-1.13	1.76	-3.02	0.20
	S_4	0.51	1.62	2.99	12.99	-1.28	9.72
M	AV [K]	259.76	9.04	-0.13	-0.45	234.80	278.12
A	min [K]	214.20	6.83	0.26	0.81	198.00	235.68
R	MAX [K]	287.78	6.53	1.13	0.90	278.98	308.00
	S_2 [K]	16.05	4.81	0.22	-0.10	5.87	29.55
	S_3	-0.67	0.67	-1.95	10.68	-4.78	0.61
	S_4	0.24	3.24	7.65	68.52	-1.75	30.73
A	AV [K]	265.77	5.97	-1.24	2.59	244.74	274.99
P	min [K]	219.05	7.41	-0.39	0.52	198.00	235.24
R	MAX [K]	290.51	7.97	0.46	-1.13	279.85	308.00
	S_2 [K]	13.66	3.97	0.57	0.22	6.98	24.87
	S_3	-0.79	0.46	0.59	0.47	-1.54	0.54
	S_4	0.24	1.12	1.12	1.60	-1.37	3.91
A	AV [K]	261.58	7.74	-0.49	0.25	234.80	278.12
L	min [K]	216.42	7.15	-0.04	0.47	198.00	235.68
L	MAX [K]	287.49	6.74	1.23	0.90	278.12	308.00
	S_2 [K]	14.42	4.37	0.70	0.45	5.87	29.55
	S_3	-0.72	0.61	-1.53	8.26	-4.78	0.61
	S_4	0.33	2.54	8.36	94.30	-1.75	30.73

9. NOAA-11 DT4 and DT5 correction [K] for the GPCP-AIP/2 data set.

T	DT4	DT5
205	1.11	-1.22
215	0.66	-1.17
225	0.29	-1.05
235	0.09	-0.95
245	0.07	-0.85
255	-0.19	-0.72
265	-0.34	-0.49
275	-0.11	-0.33
285	-0.10	-0.08
295	0.05	0.27
305	0.32	0.65
310	0.46	0.86
315	0.65	1.05
320	0.79	1.27

10. GPCP-AIP/2 selected passes.

Date	Time(s) (GMT)			
08/Feb/91	02:58			
16/Feb/91	18:31			
21/Feb/91	18:15			
24/Feb/91	18:46			
06/Mar/91	18:15			
08/Mar/91	02:46	07:42	14:18	17:29
17/Mar/91	02:45	07:34		
18/Mar/91	18:37			
21/Mar/91	17:28	19:07		
25/Mar/91	07:48	19:15		
26/Mar/91	02:44	07:25	14:17	18:51
01/Apr/91	03:17	08:26		
02/Apr/91	19:29			
04/Apr/91	02:43	07:16	12:35	18:42

LIST OF FIGURES

21. AVHRR-CH4, APR: SUMMARY+CUM

    (The circled points in frame B are the GPCP-AIP/2 selected cases).

22. AVHRR-CH5, FEB: SUMMARY

23. AVHRR-CH5, MAR: SUMMARY

24. AVHRR-CH5, APR: SUMMARY+CUM

25. Typical calibration curves (*solid line*) for AVHRR channels 3 (A) and 4 (B) (the curve for channel 5 is very similar to the curve for channel 4) 10-bit digital counts (lower scale) to brightness temperature (adapted from d'Entremont and Kleespies, 1988) and correspondent 8-bit digital counts (upper scale) to brightness temperature curves (*dashed line*) adopted for the GPCP-AIP/2 AVHRR data set.

26. Example of single scatterplots T4 (*ordinate*) T3 (*abscissa*) for the images available on the 19/03/91 (GMT time). The limits of both the axis are $198 \div 308$ K.

27. Correction factors (DT [K]) to be added to the GPCP-AIP/2 NOAA-11 data set:

    A) T4; B) T5; C) T4-T5.

    The limits of the ordinate are $-2.0 \div +3.0$ K. The curves relative to T4 have been computed assuming the same baseplate temperature for NOAA-10 as for NOAA-11. The correction for T4-T5 is approximate because of the hypothesis T5=T4 used for the computation of the correction factors (see text). Each curve is relative to an internal blackbody temperature ([——]: 282.35 K, [– – –]: 287.35 K, [–.–.–]: 292.15 K]).

28. Example of single images scatterplots T4-T5 vs T4 for two of the GPCP-AIP/2 selected cases (91/03/08-02:46 (*lower panels*), 91/03/26-02:44 (*upper panels*)). The limits of the axis are $198 \div 300$ K for the abscissa and $-5 \div 12.5$ K for the ordinate. The scatterplots on the left have been plotted using uncorrected GPCP-AIP/2 data, the one on the right using the correction shown in Fig.27.

29. Example of statistics from T4-T5 images for two of the GPCP-AIP/2 selected cases (91/03/08-02:46 (*lower panel*), 91/03/26-02:44 (*upper panel*)). The histogram classes are 1 K wide and the value reported on the abscissa represent the upper limit (not included). The right bins [▨] are relative uncorrected GPCP-AIP/2 data, the left one [▩] are relative to the corrected image.

30. Example of 2-values images [black: $T4 < T5$, white: $T4 > T5$] for two of the GPCP-AIP/2 selected cases (91/03/08-02:46 (*lower panels*), 91/03/26-02:44 (*upper panels*)). For the images on the left uncorrected GPCP-AIP/2 data have been used, for the one on the right corrected (see text).

31. Percent difference ($D = 100. * (A_{Autosat2} - A_{NOAA})/A_{NOAA}$) between the albedo as computed for the GPCP-AIP/2 and the one obtained using the NOAA (Appendix B, Lauritson et al. 1988) calibration coefficients. The curves are computed for solar zenith angles of: 88°, 80°, 70°, 60°, 50° and 40° (being the 88° one the most external and the 40° the internal). Only values of $|D| < 100\%$ have been plotted.

    A) NOAA-11 CH1 B) NOAA-11 CH2

    C) NOAA-10 CH1 D) NOAA-10 CH2.

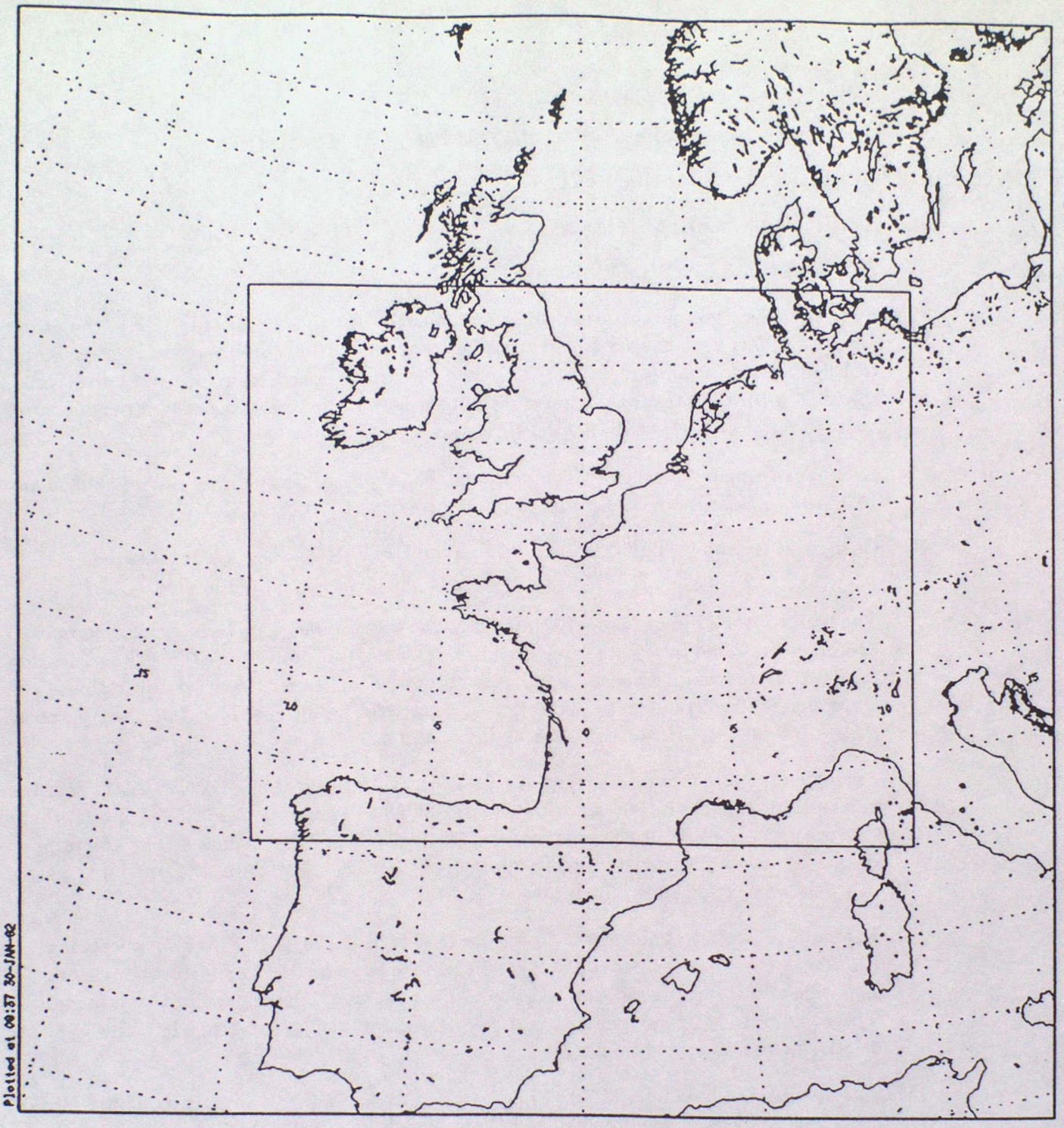

1. GPCP-AIP/2 Area (internal frame).

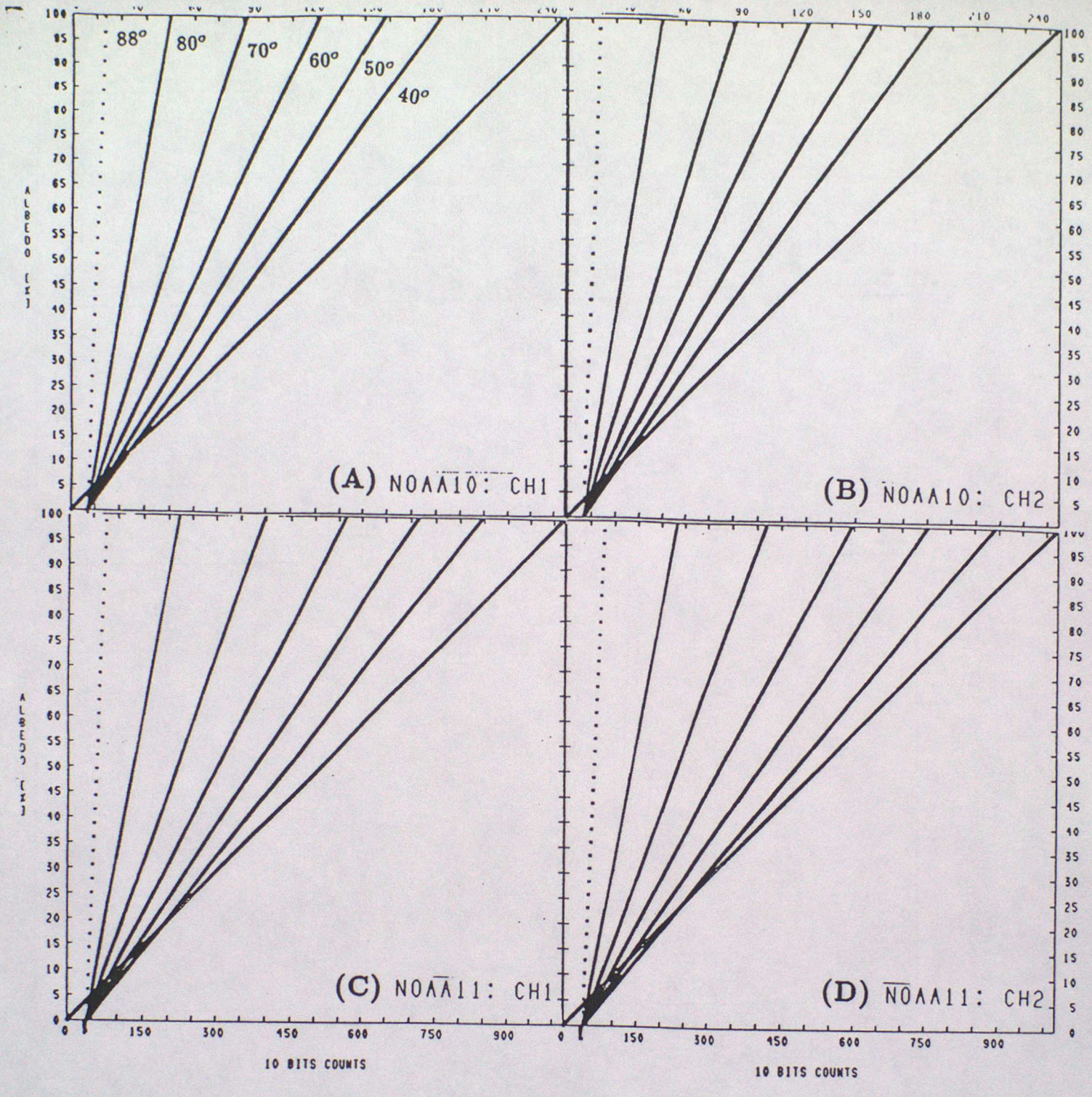

2. Typical 10-bit-count-albedo [x - *lower scale*] relationships for AVHRR visible channels (eq.1). The curves are computed for solar zenith angles (ϕ) of: 88°, 80°, 70°, 60°, 50° and 40°. The figure also shows the GPCP-AIP/2 8-bit-count-albedo [o - *upper scale*] relationship.

A) NOAA-10 CH1 B) NOAA-10 CH2

C) NOAA-11 CH1 D) NOAA-11 CH2.

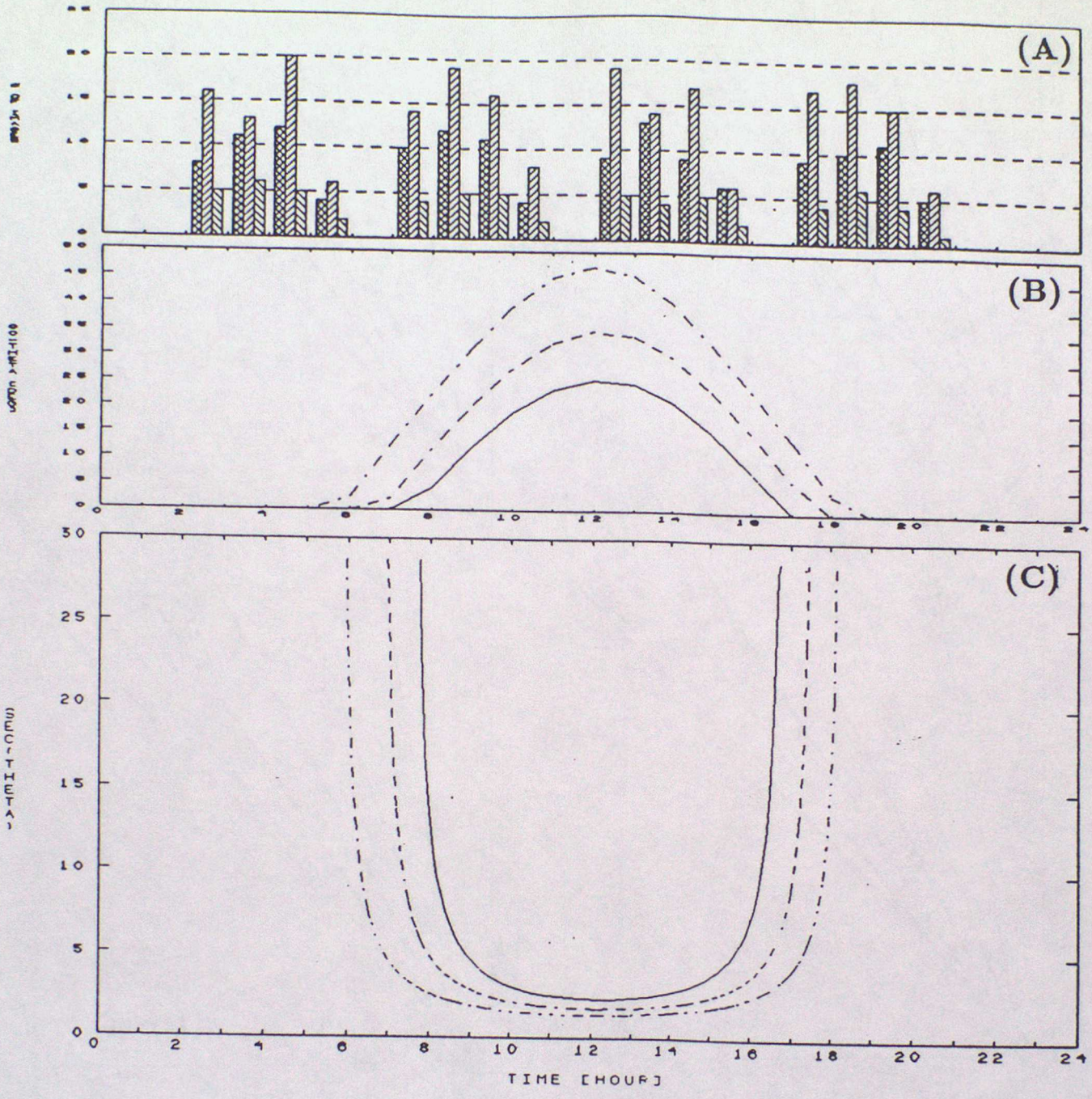

3. A) Hourly distribution of channel 3 images for the 3 months ordered from the left. (February ▩, March ▨, April ▧)

   B) Solar elevation angle ($90° - \phi$ [deg]) calculated at 47°N-0°E. for:

   1st February [——], 1st March [- - -], 1st April [-·-·-]

   C) Secant of the solar zenith angle (secϕ) calculated at 47°N-0°E for:

   1st February [——], 1st March [- - -], 1st April [-·-·-].

4. AVHRR-CH1, FEB: SUMMARY

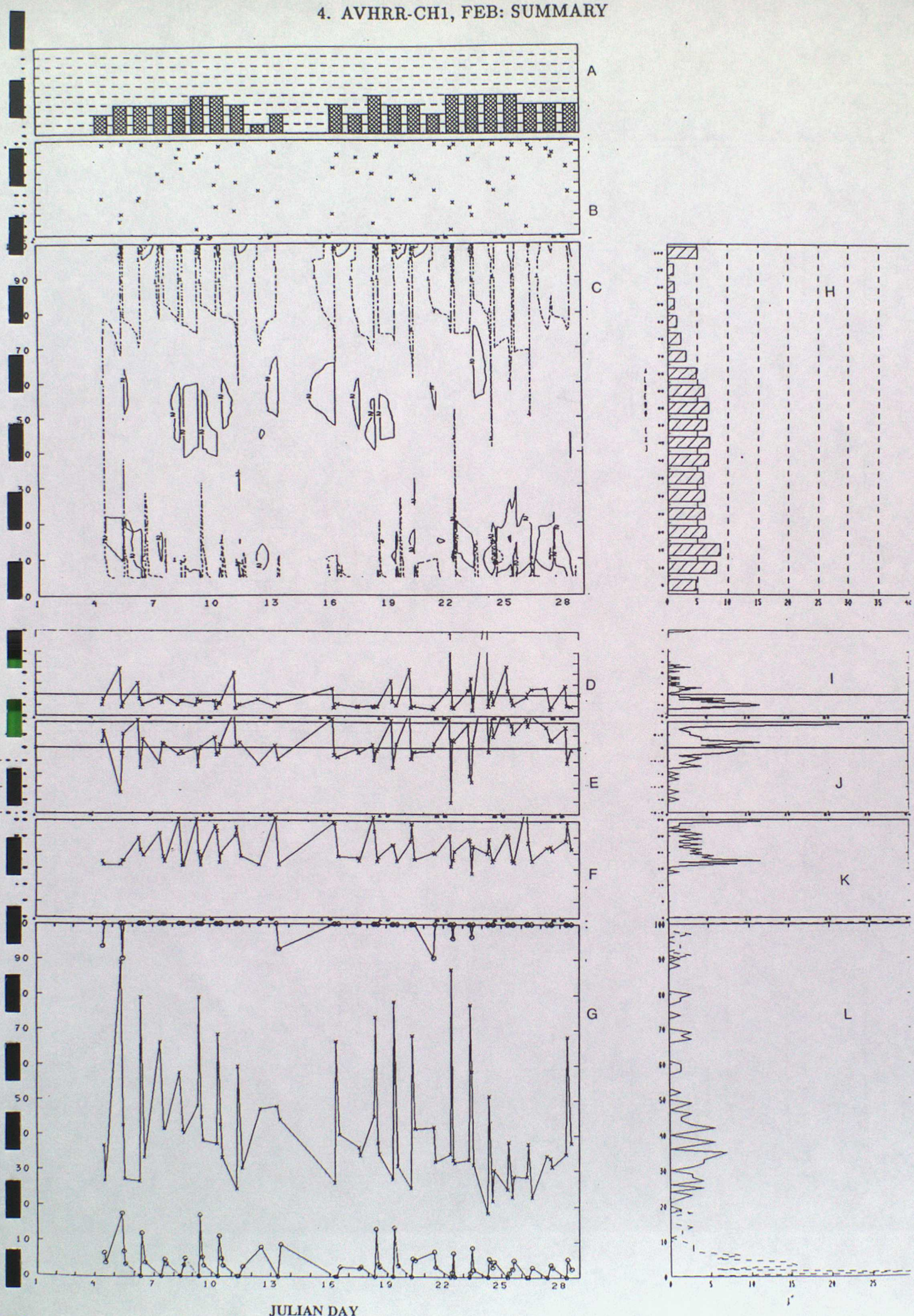

5. AVHRR-CH1, MAR: SUMMARY

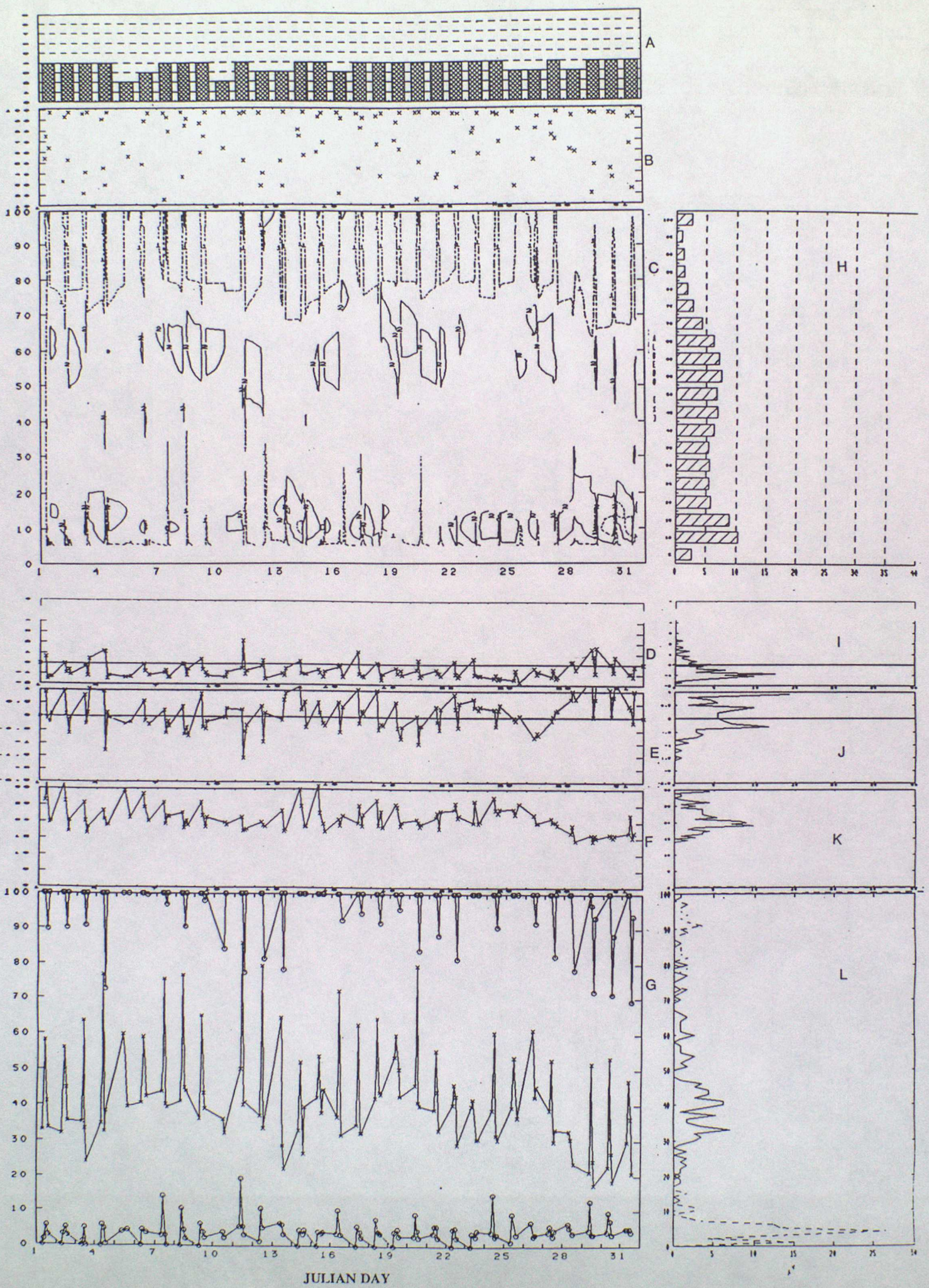

6. AVHRR-CH1, APR: SUMMARY+CUM

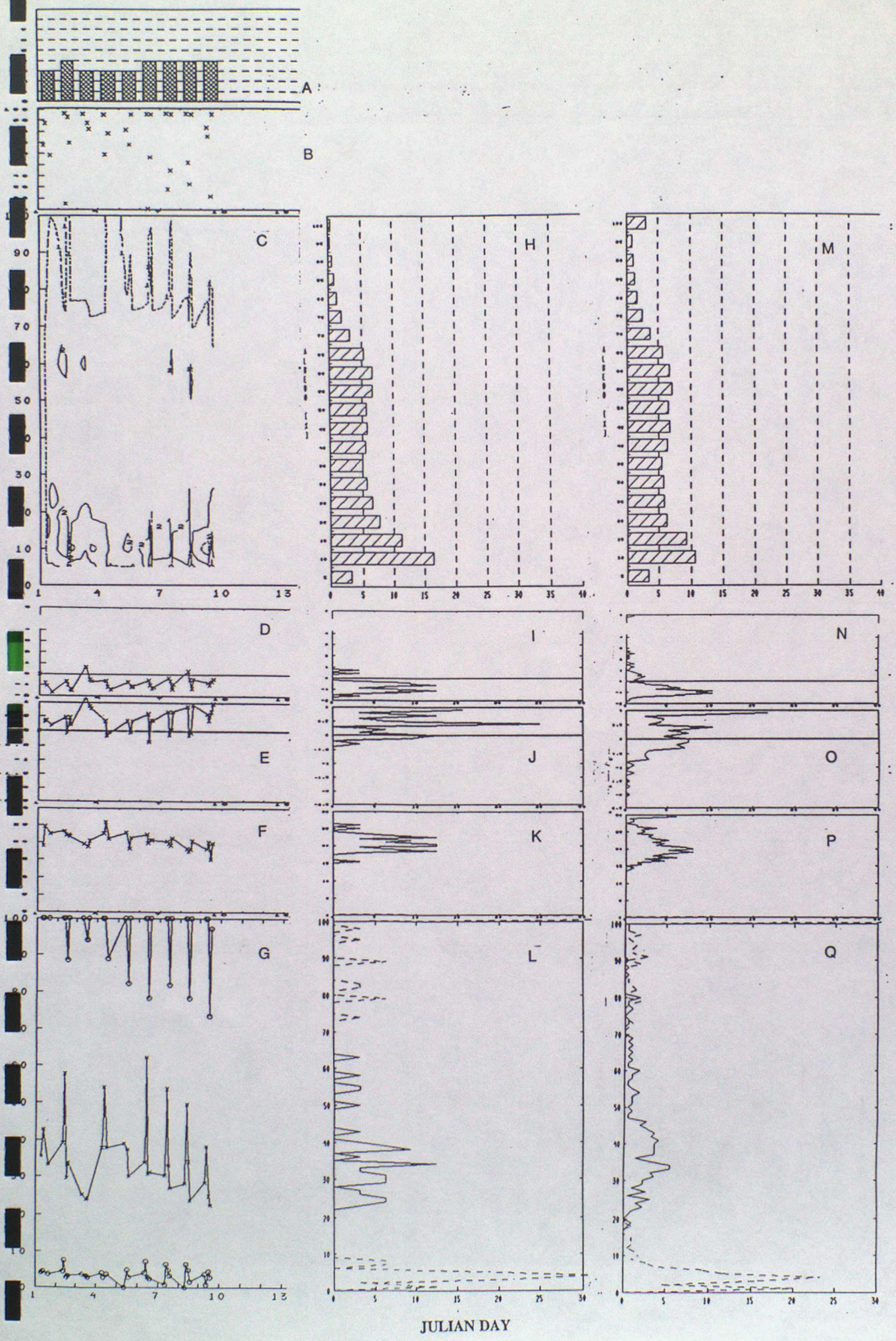

7. AVHRR-CH2, FEB: SUMMARY

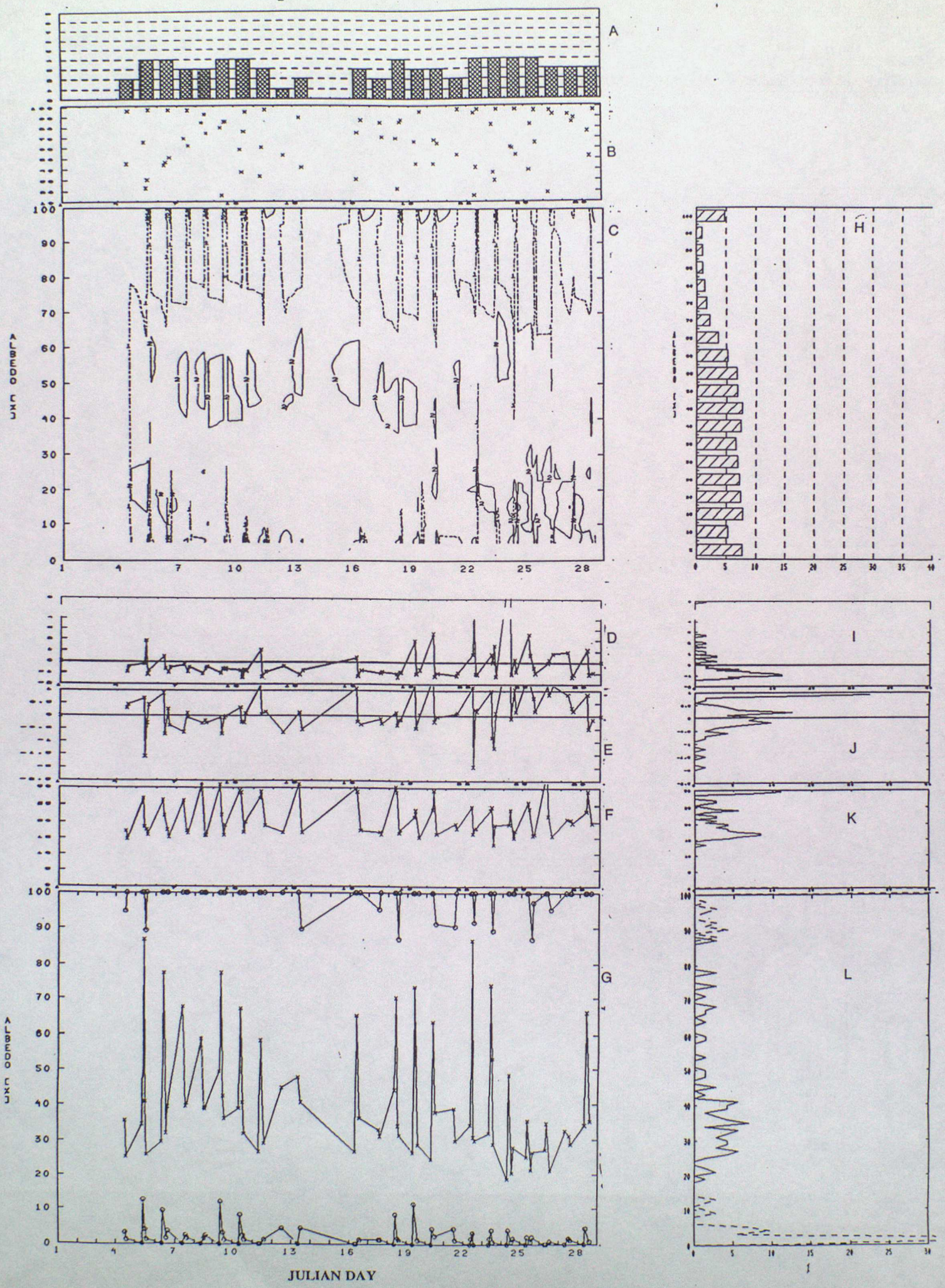

8. AVHRR-CH2, MAR: SUMMARY

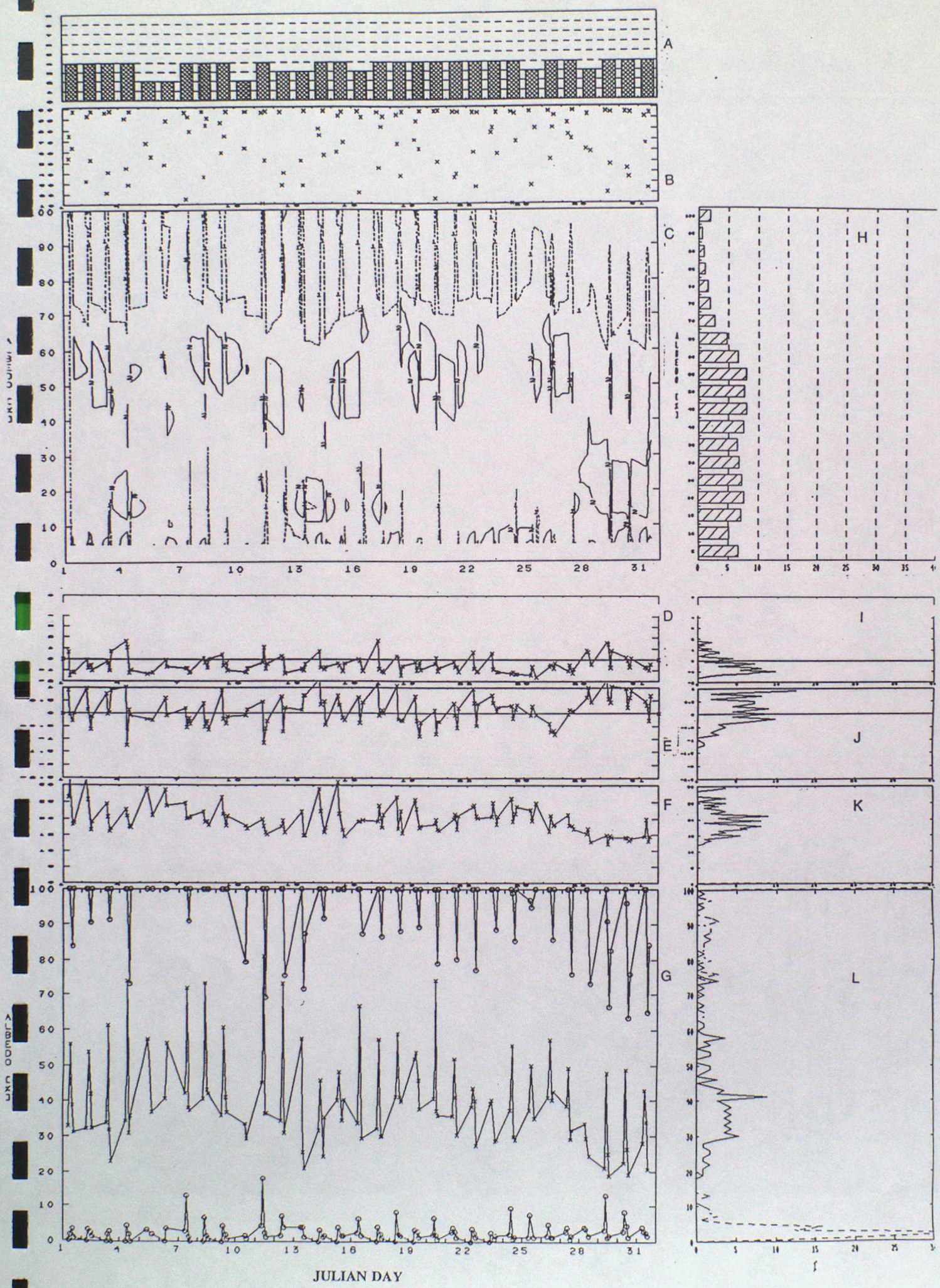

9. AVHRR-CH2, APR: SUMMARY+CUM

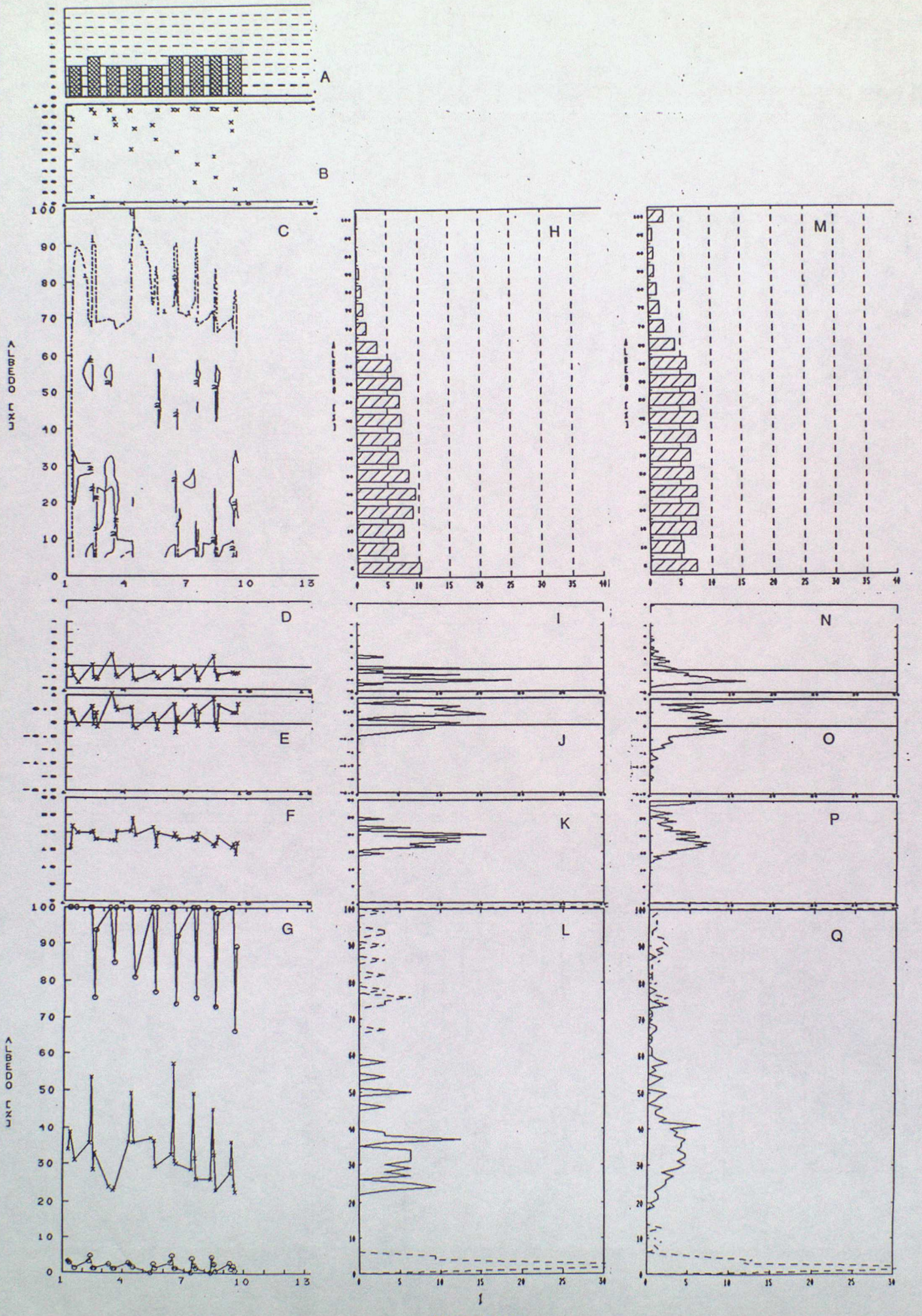

10. AVHRR-CH3$_d$, FEB: SUMMARY

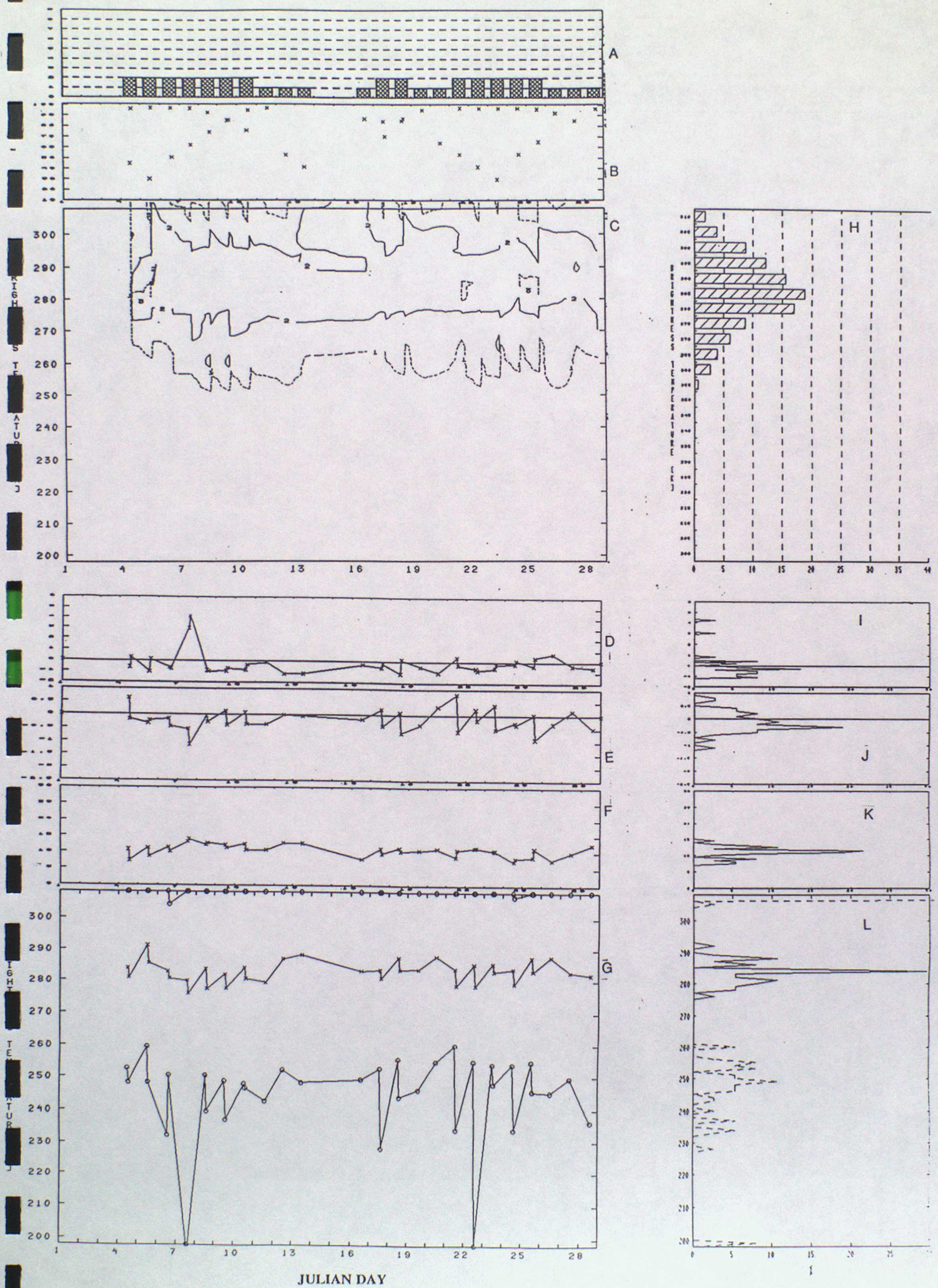

11. AVHRR-CH3$_d$, MAR: SUMMARY

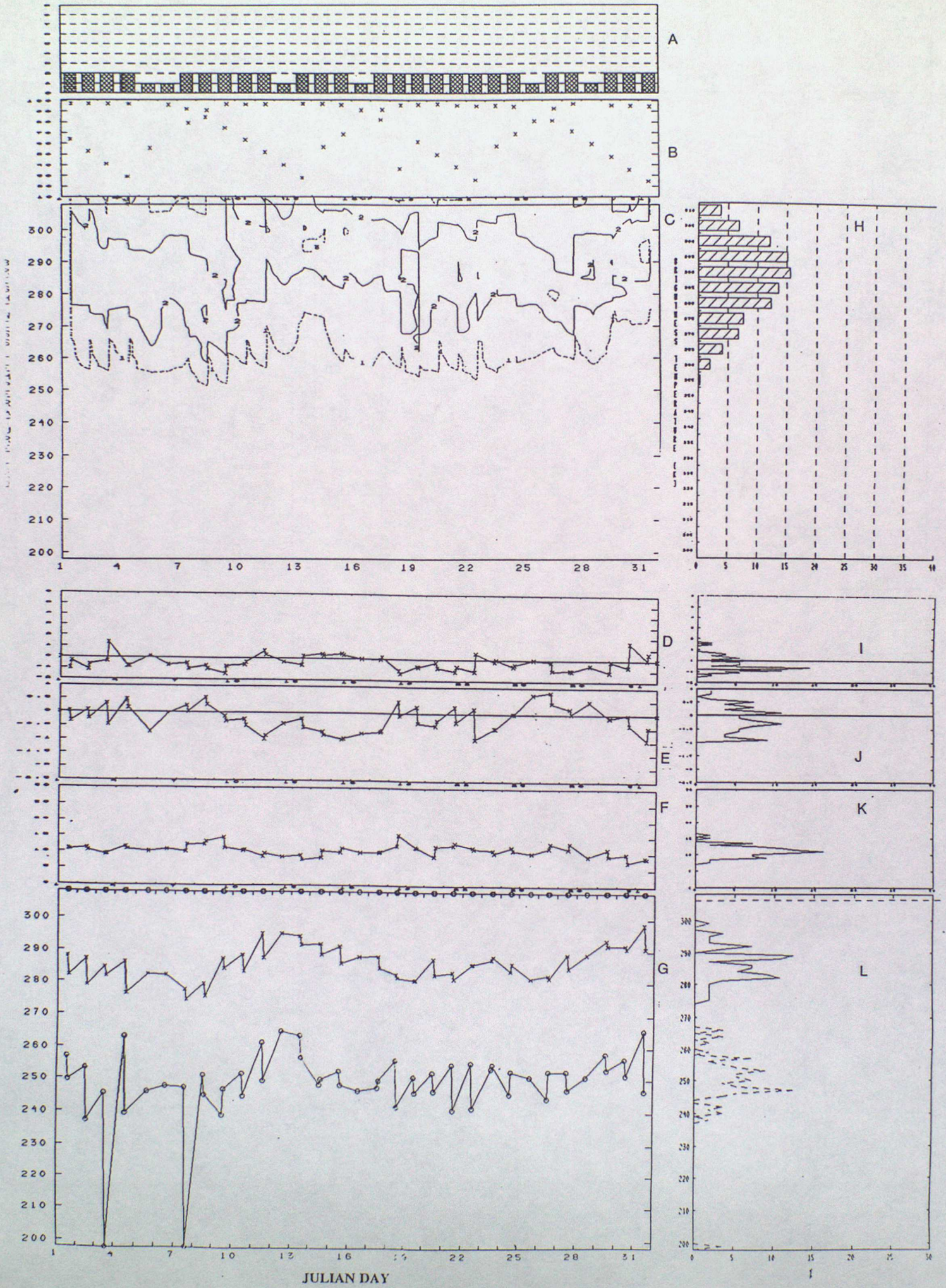

12. AVHRR-CH3$_d$, APR: SUMMARY+CUM

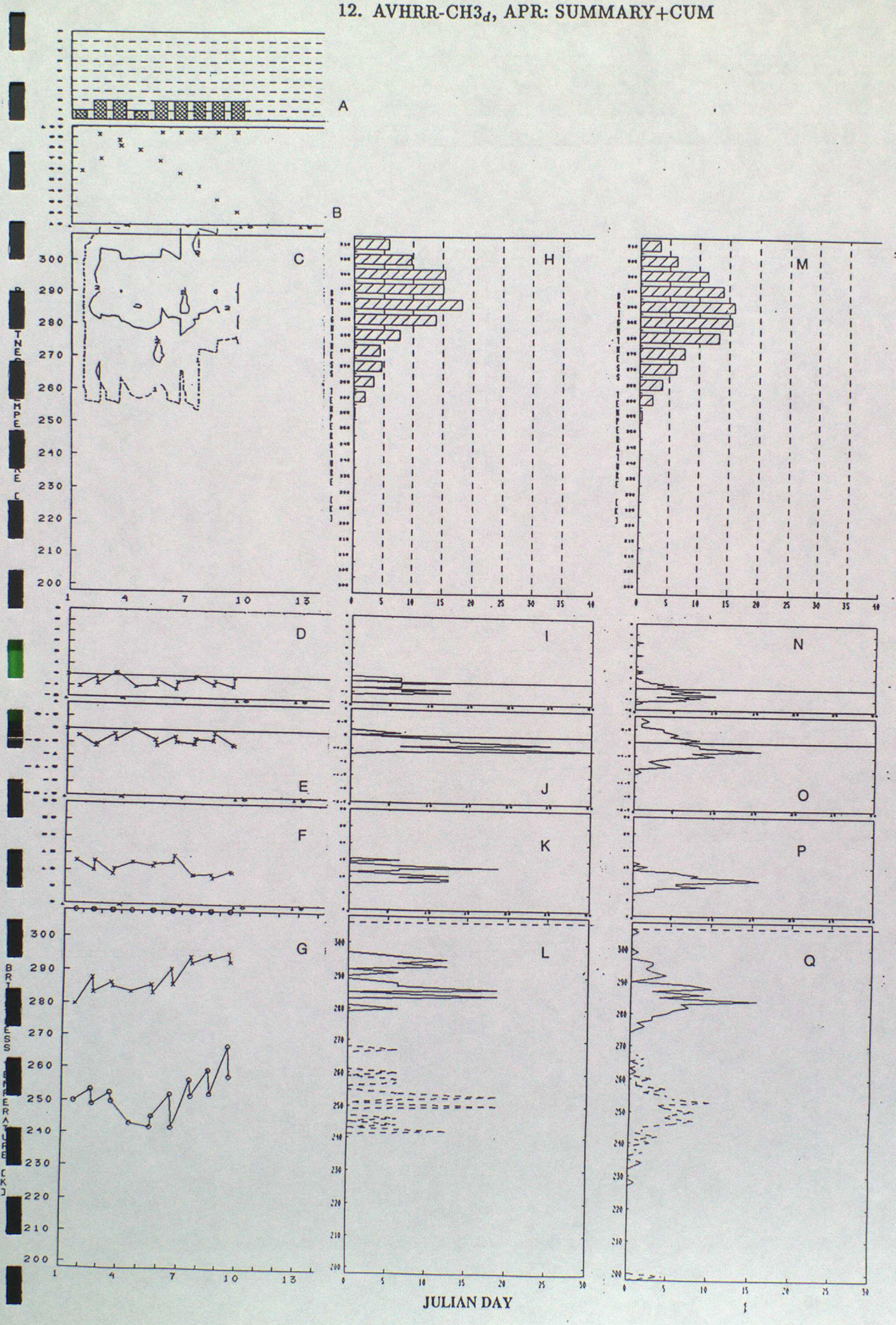

13. AVHRR-CH3$_n$, FEB: SUMMARY

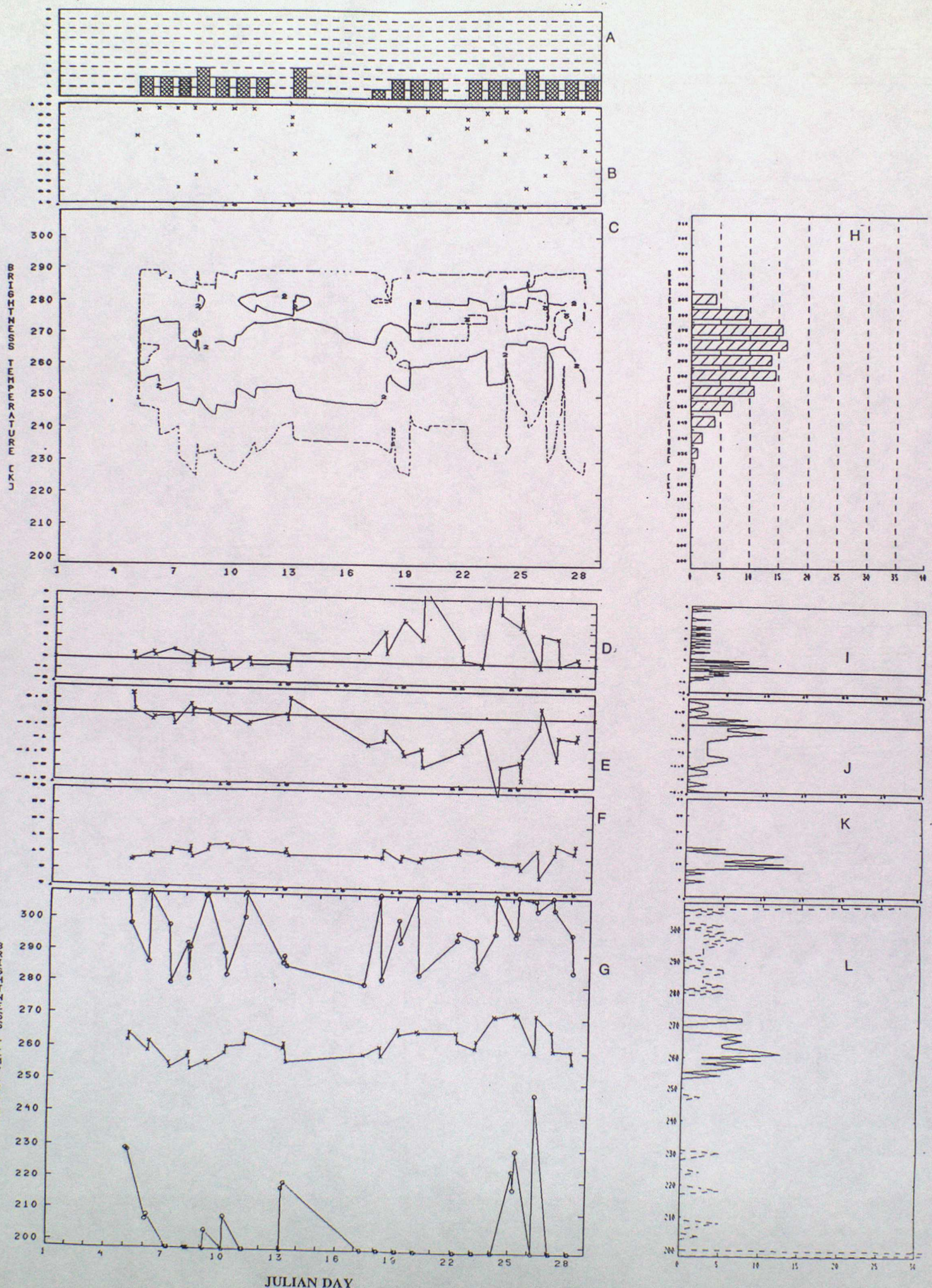

14. AVHRR-CH3$_n$, MAR: SUMMARY

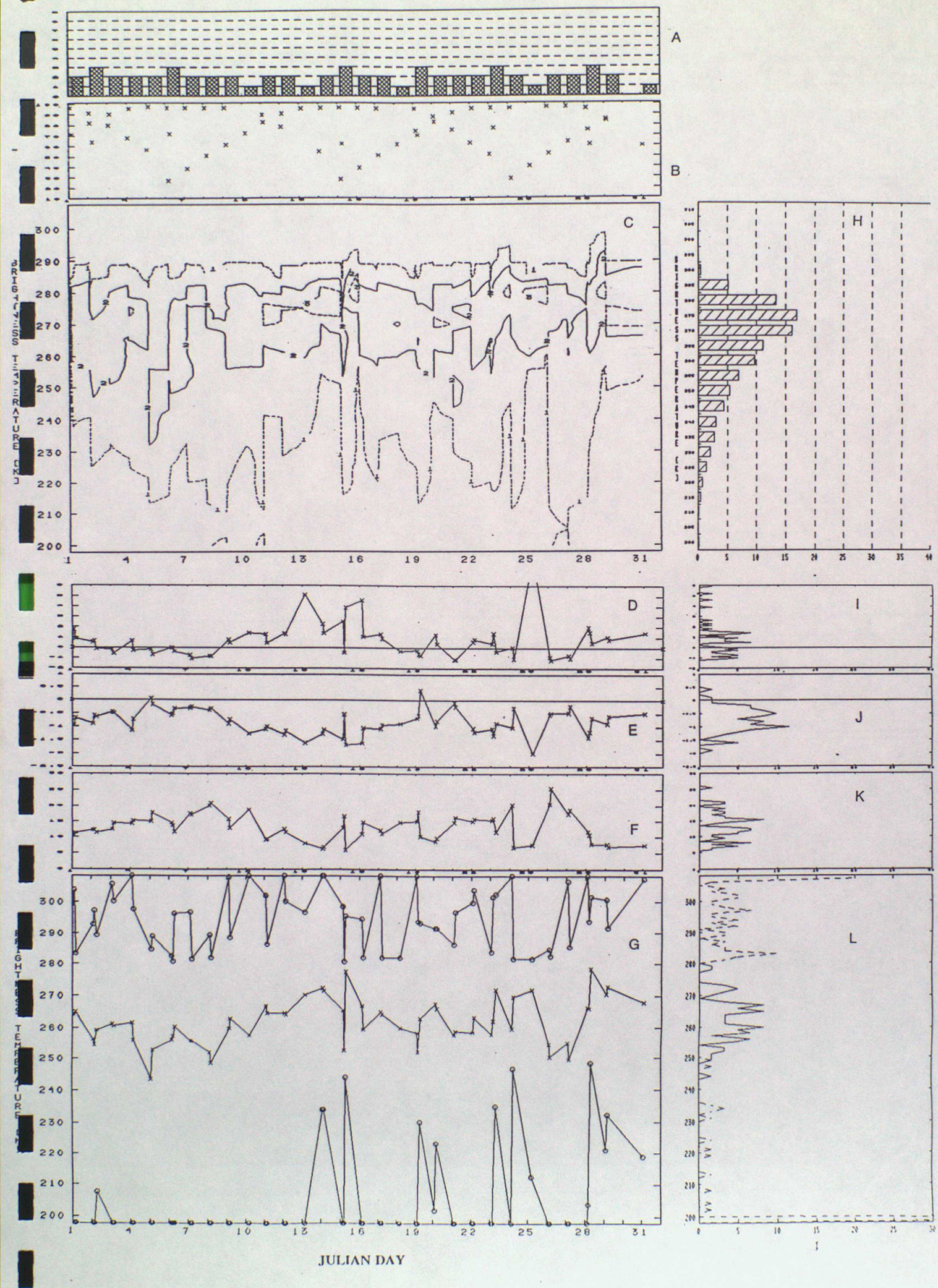

15. AVHRR-CH3$_n$, APR: SUMMARY+CUM

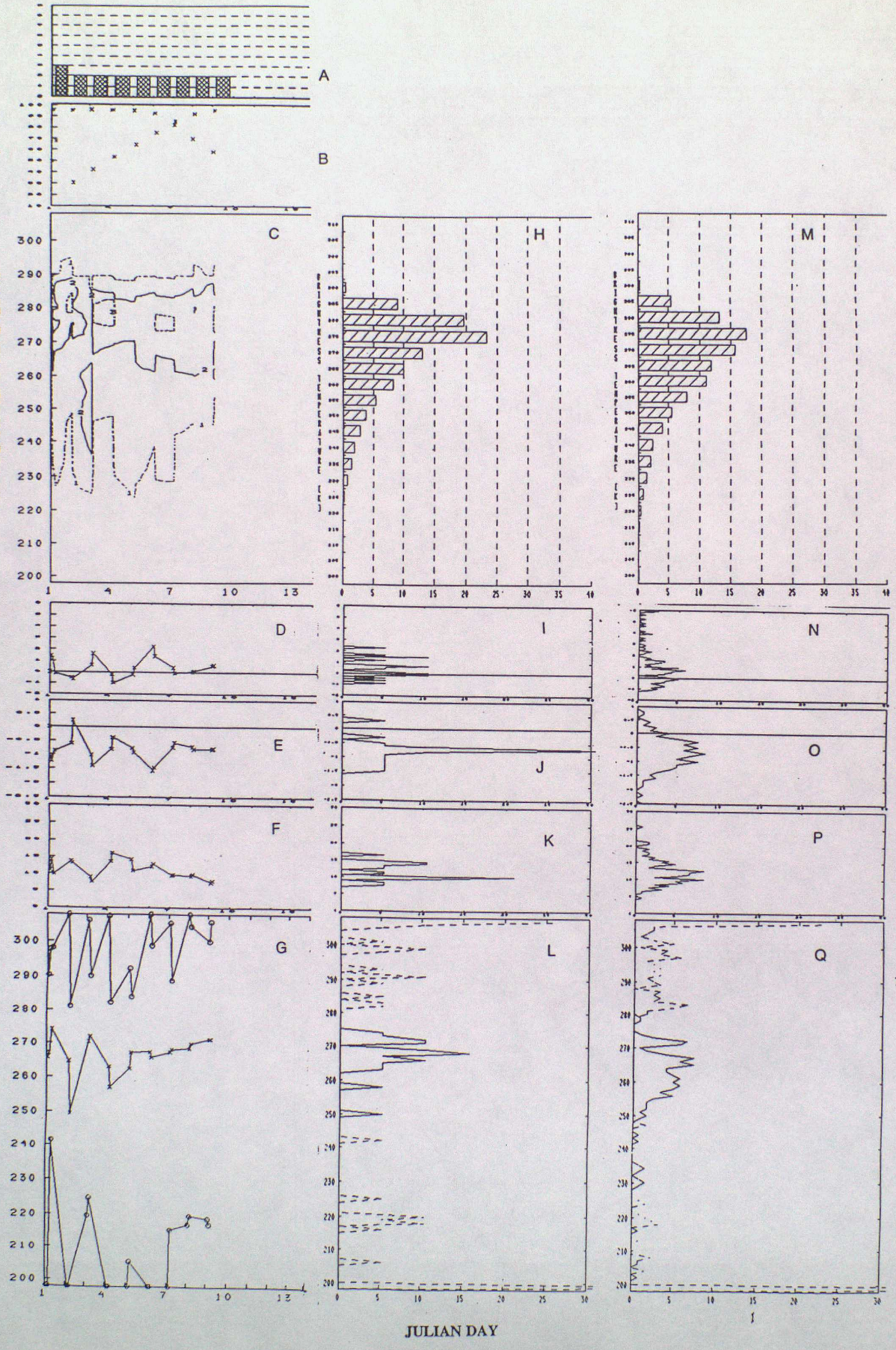

16. AVHRR-CH3$_m$, FEB: SUMMARY

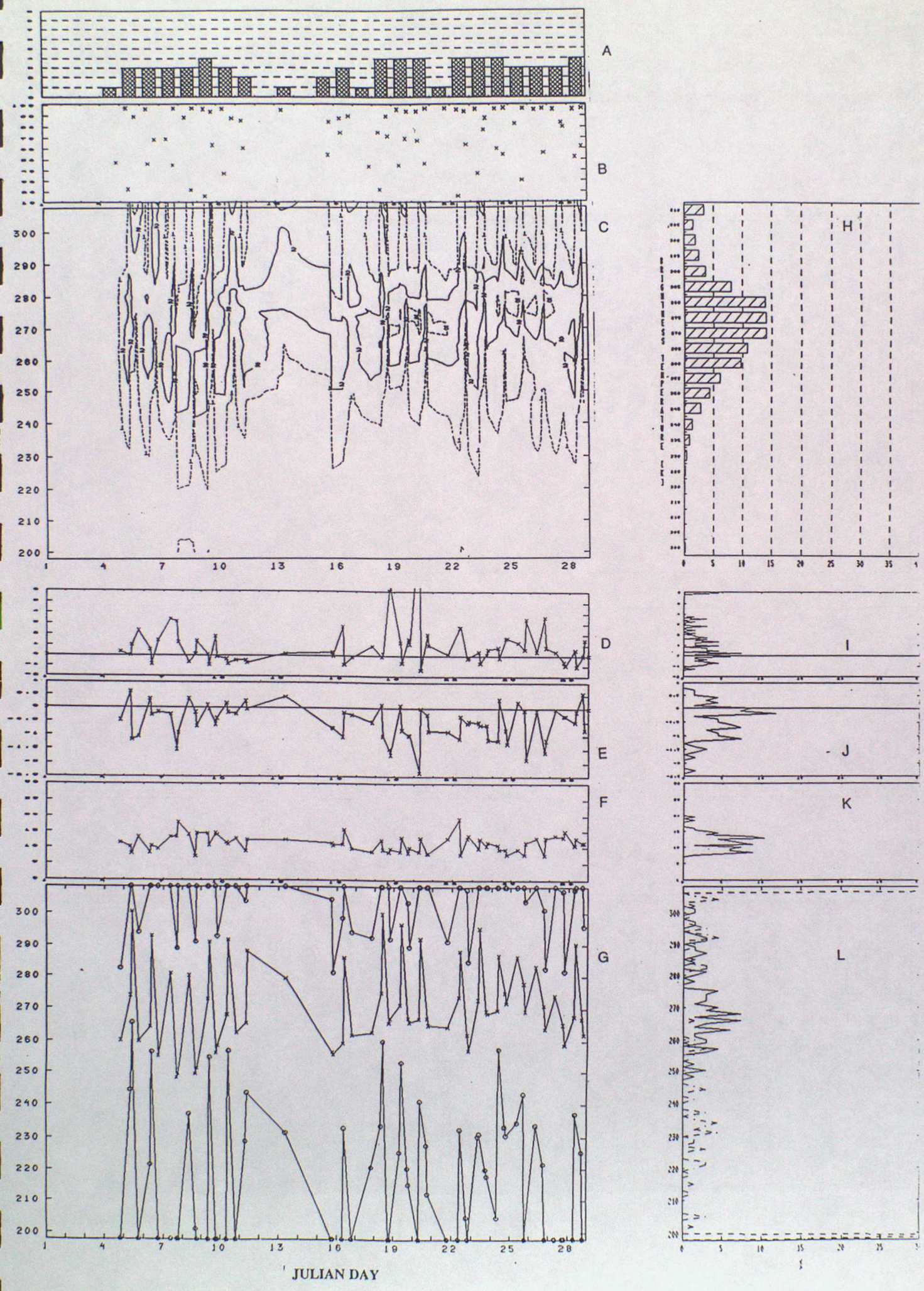

17. AVHRR-CH3$_m$, MAR: SUMMARY

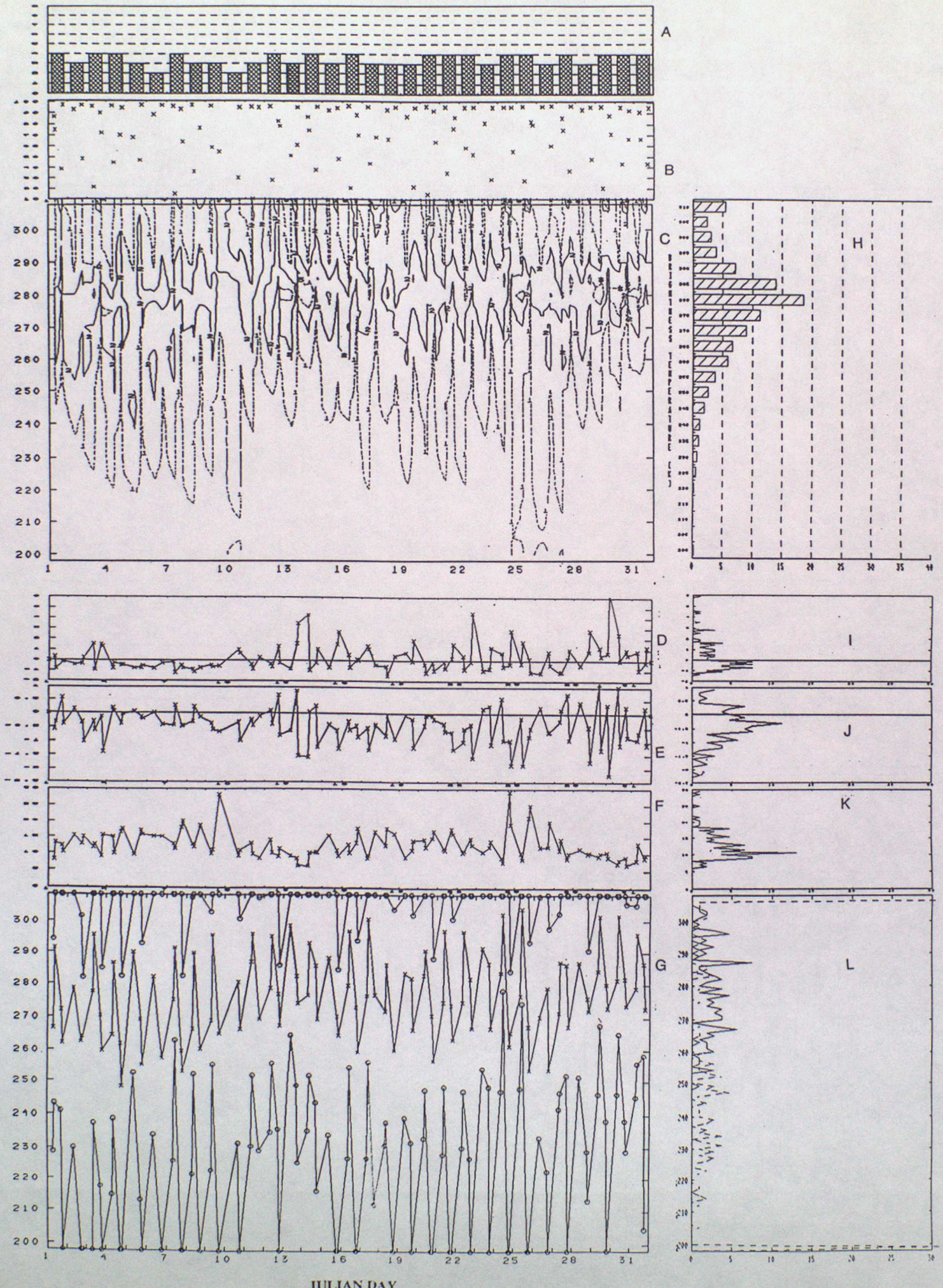

18. AVHRR-CH3$_m$, APR: SUMMARY+CUM

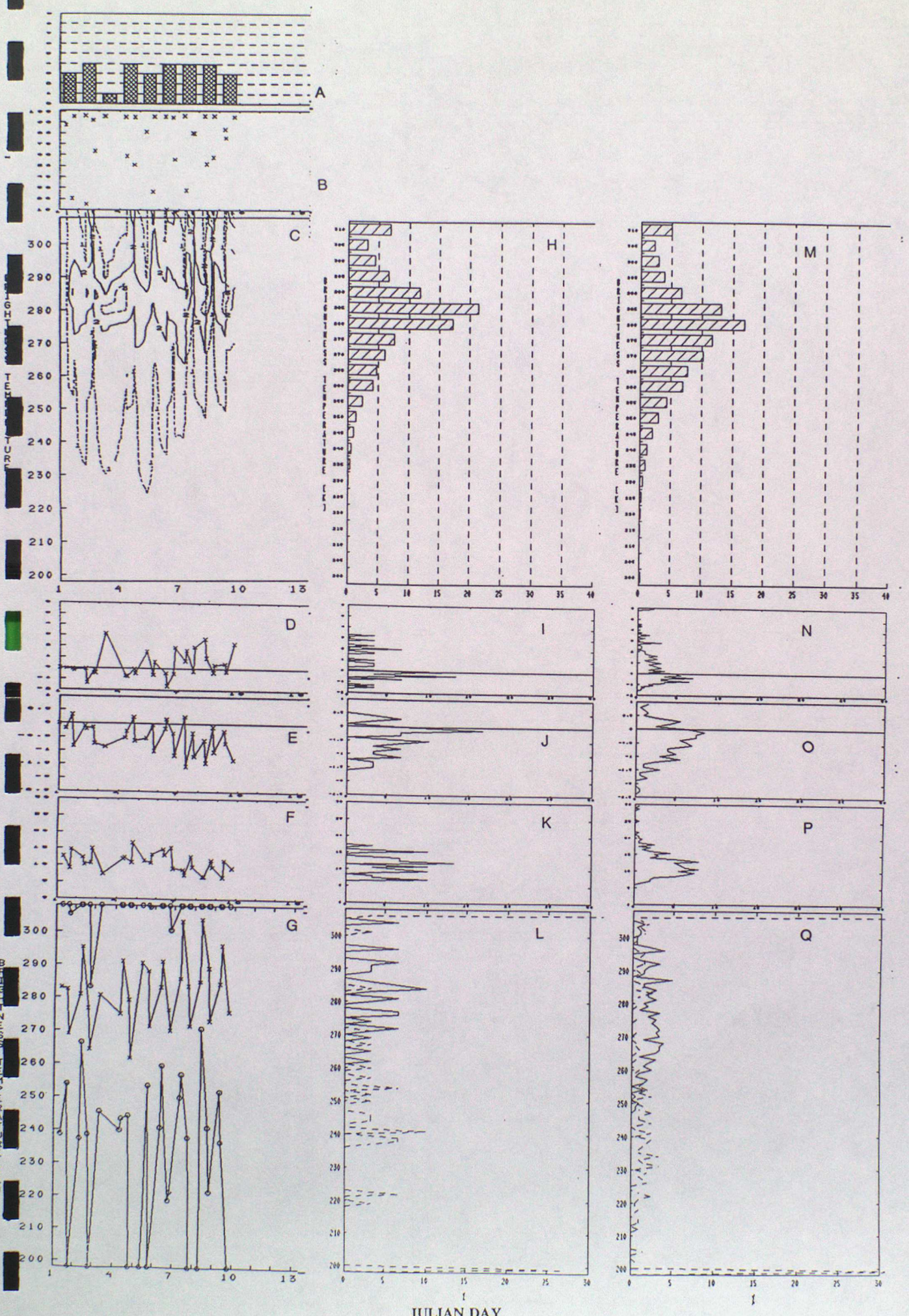

19. AVHRR-CH4, FEB: SUMMARY

(The circled points in frame B are the GPCP-AIP/2 selected cases).

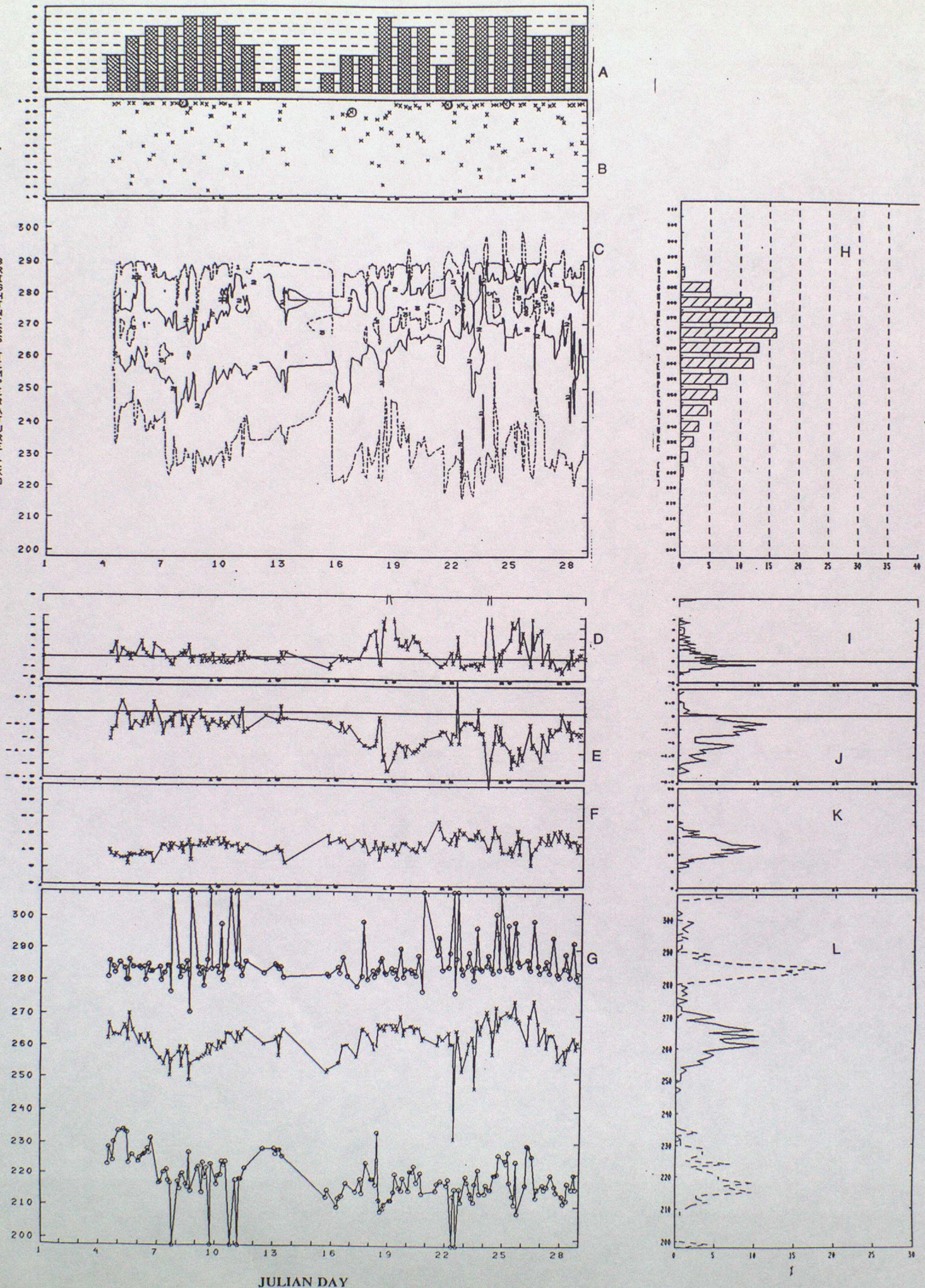

20. AVHRR-CH4, MAR: SUMMARY

(The circled points in frame B are the GPCP-AIP/2 selected cases).

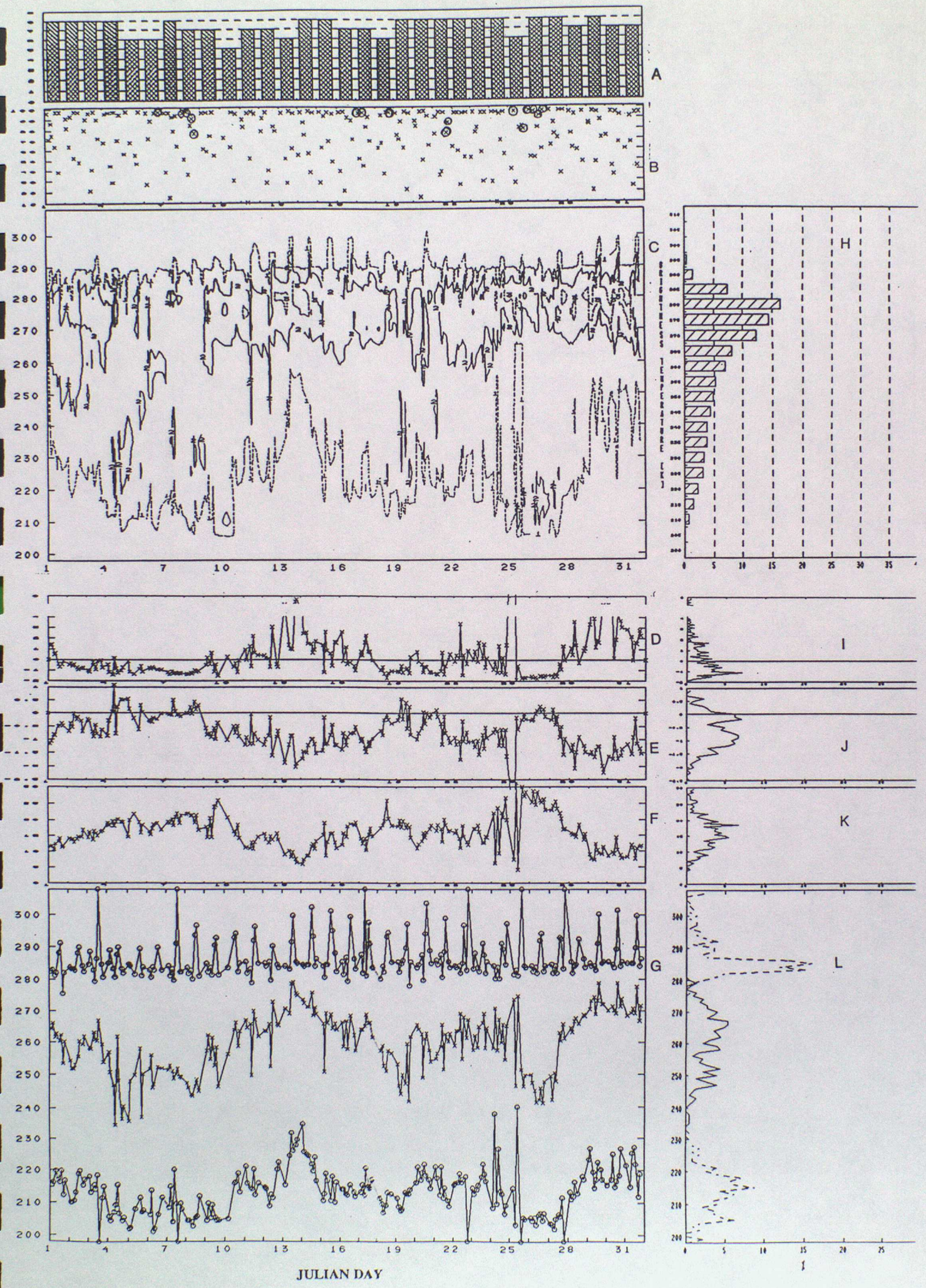

21. AVHRR-CH4, APR: SUMMARY+CUM

(The circled points in frame B are the GPCP-AIP/2 selected cases).

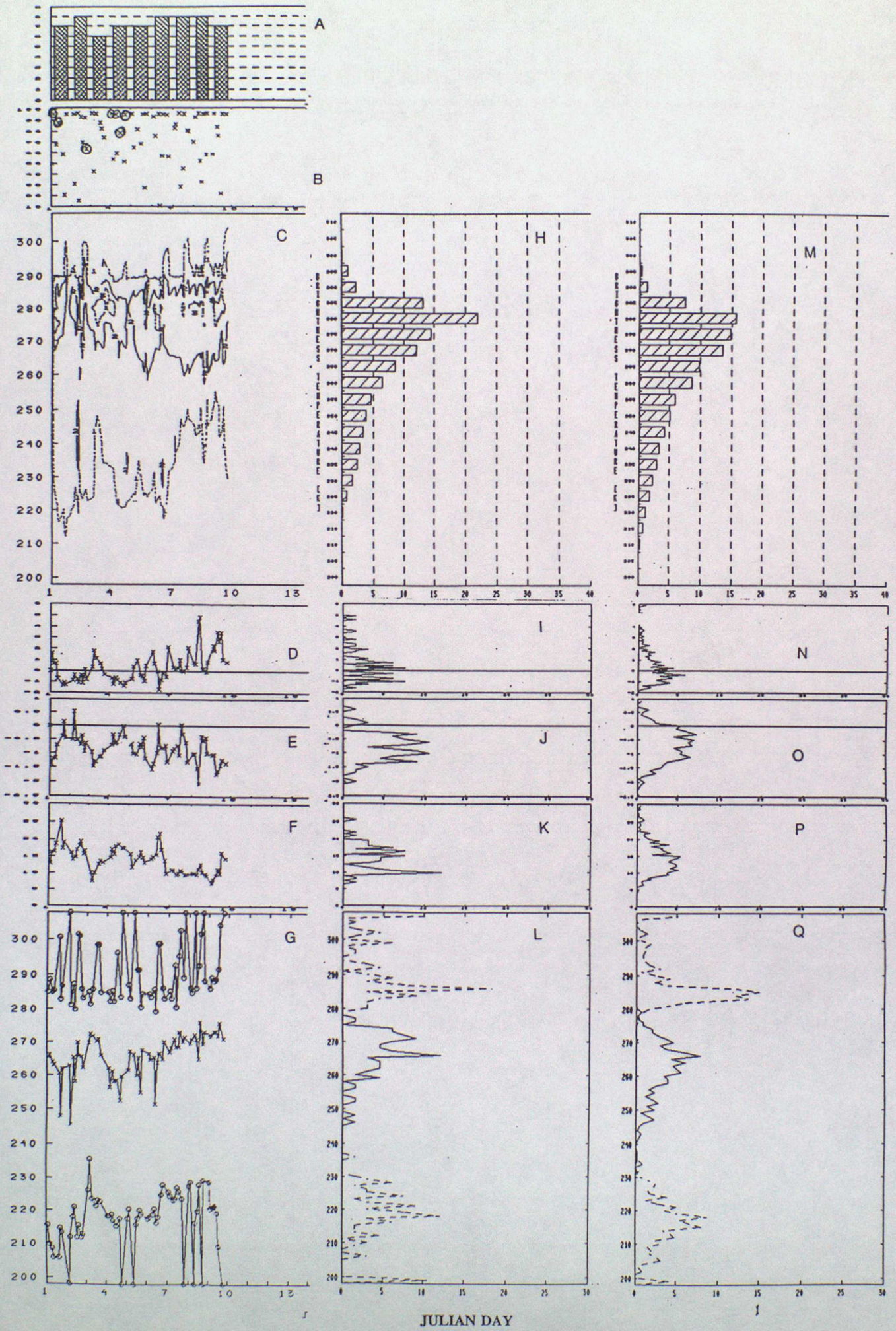

22. AVHRR-CH5, FEB: SUMMARY

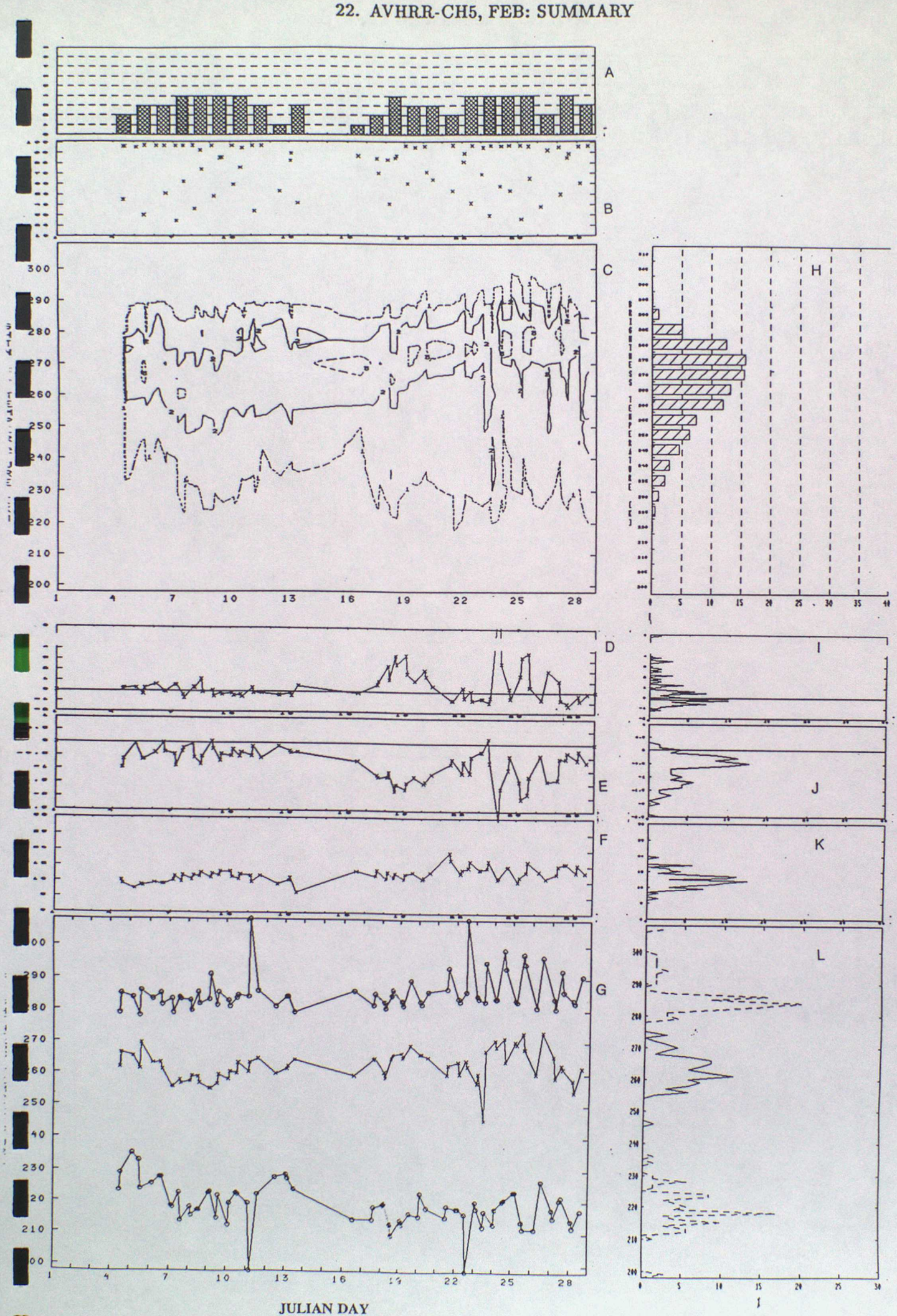

23. AVHRR-CH5, MAR: SUMMARY

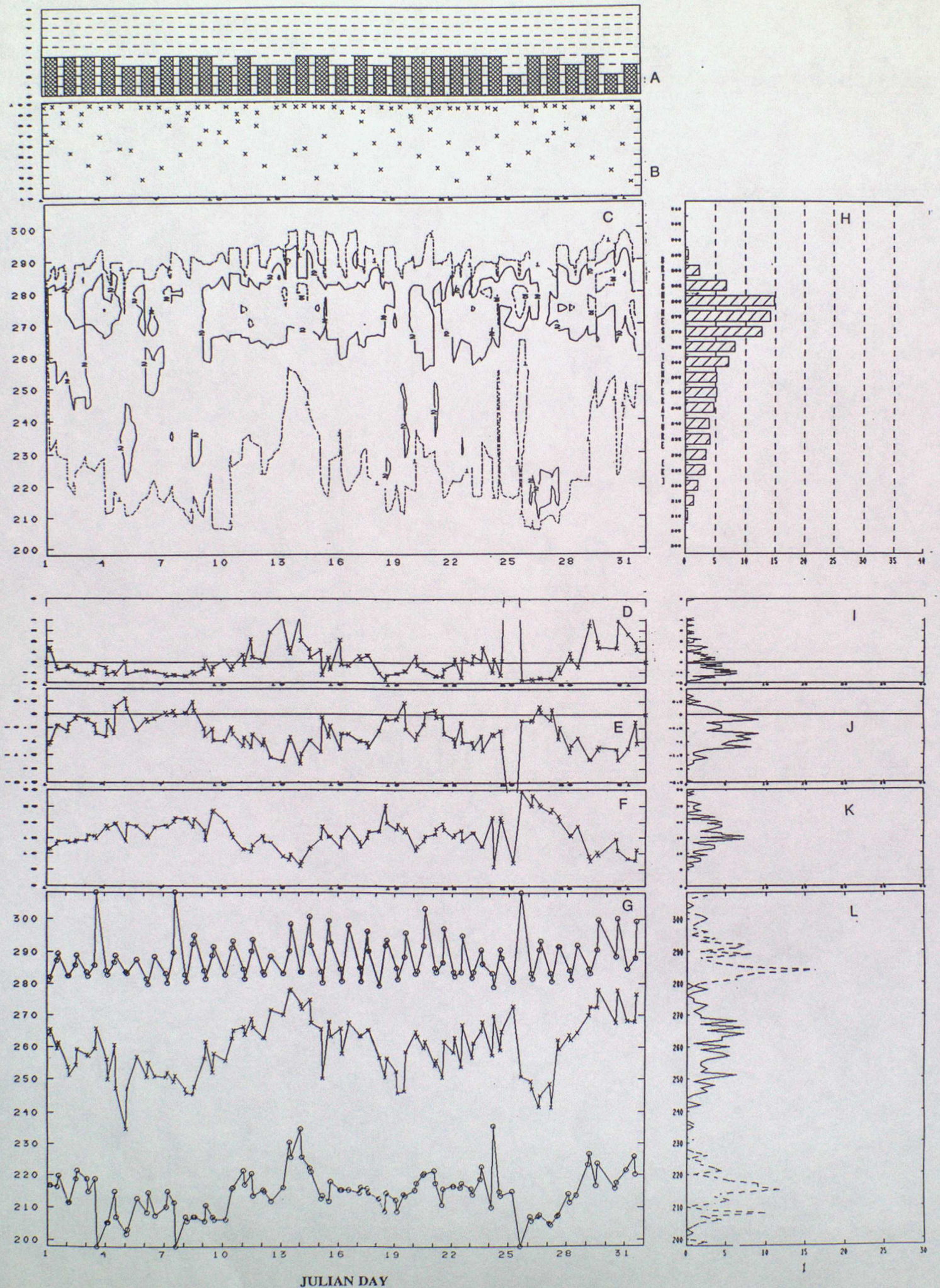

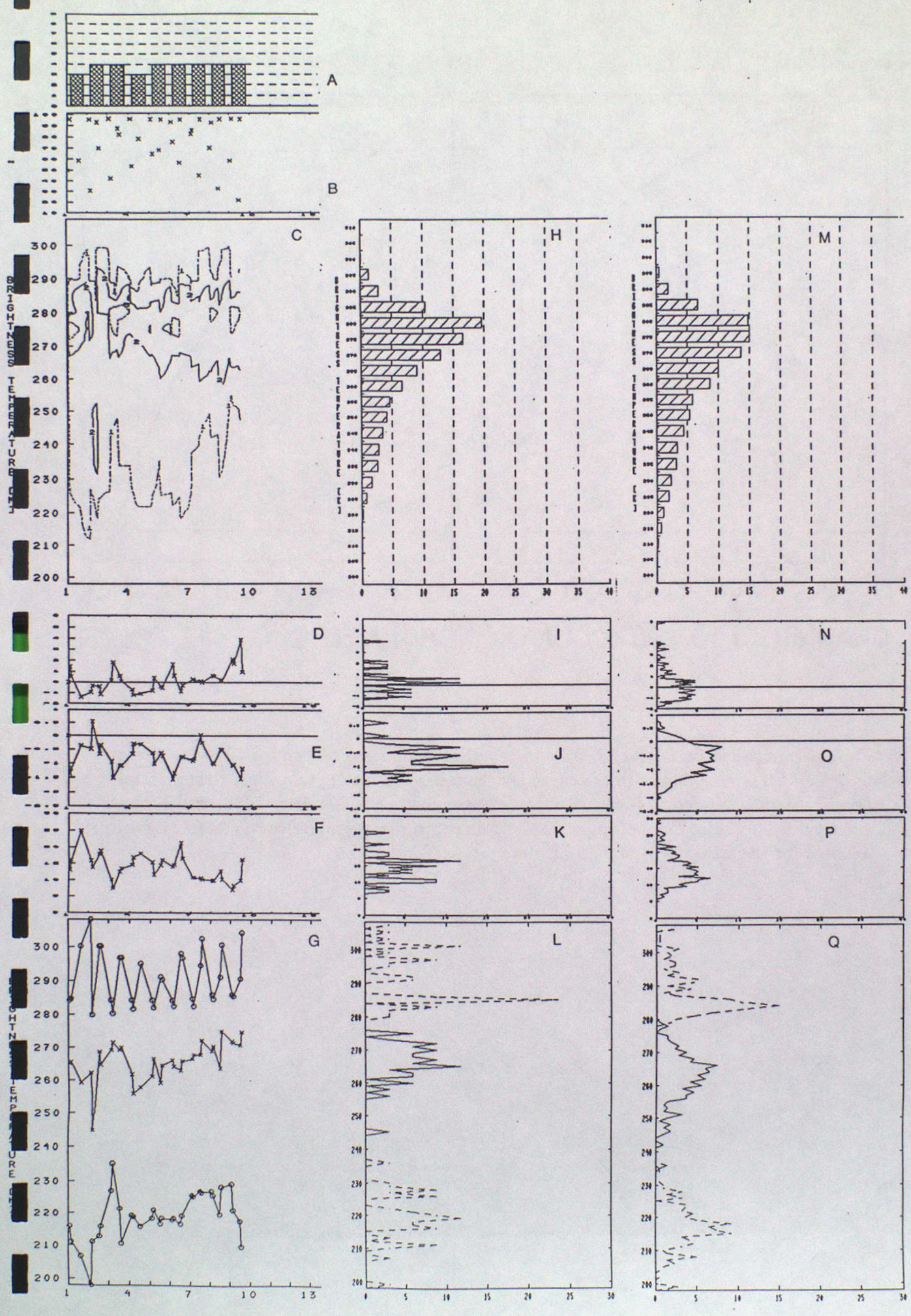
A
B
C
H
M
D
E
F
G
I
J
K
L
N
O
P
Q
BRIGHTNESS TEMPERATURE (K)
JULIAN DAY

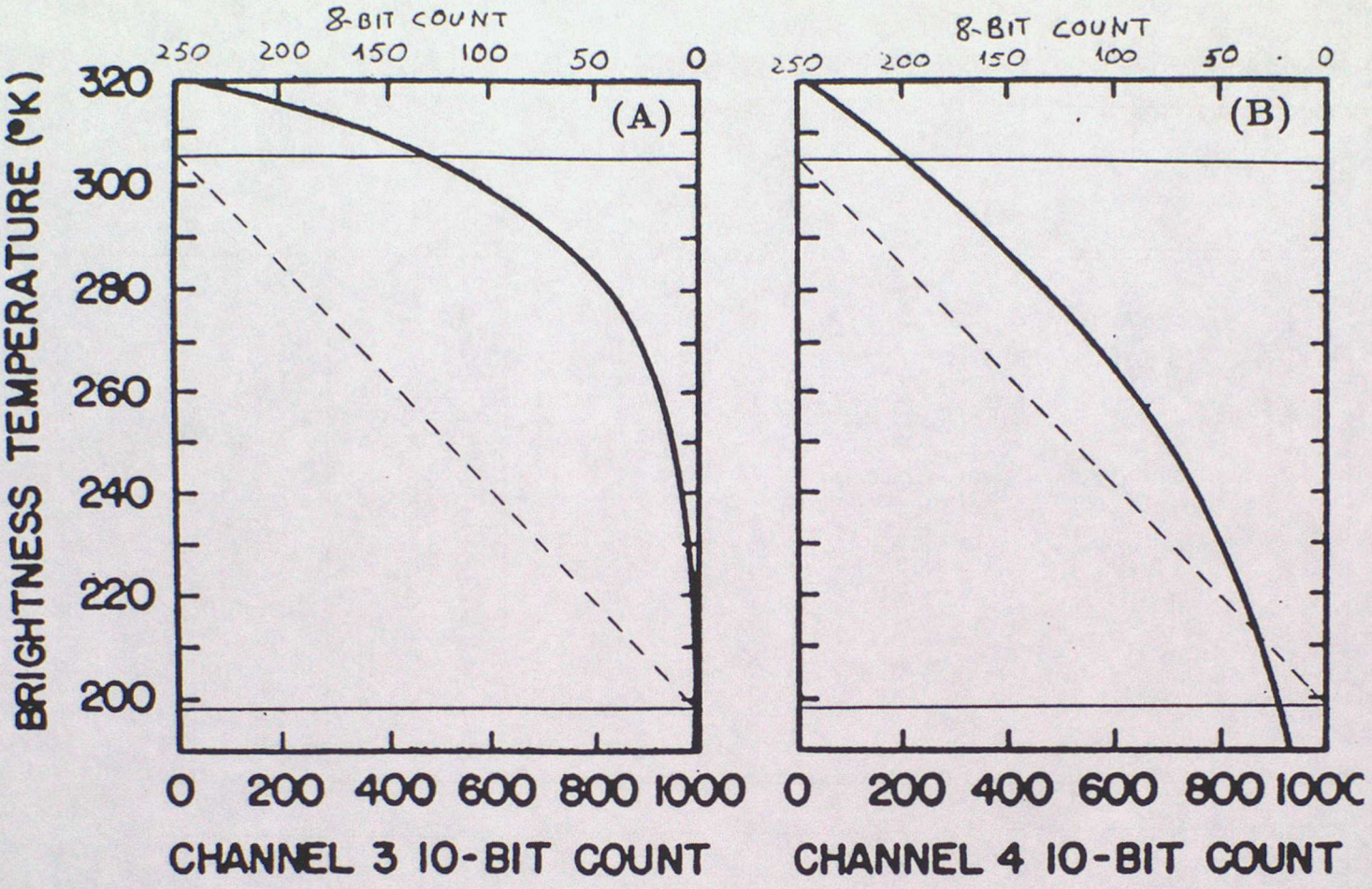

25. Typical calibration curves (*solid line*) for AVHRR channels 3 (A) and 4 (B) (the curve for channel 5 is very similar to the curve for channel 4) 10-bit digital counts (lower scale) to brightness temperature (adapted from d'Entremont and Kleespies, 1988) and correspondent 8-bit digital counts (upper scale) to brightness temperature curves (*dashed line*) adopted for the GPCP-AIP/2 AVHRR data set.

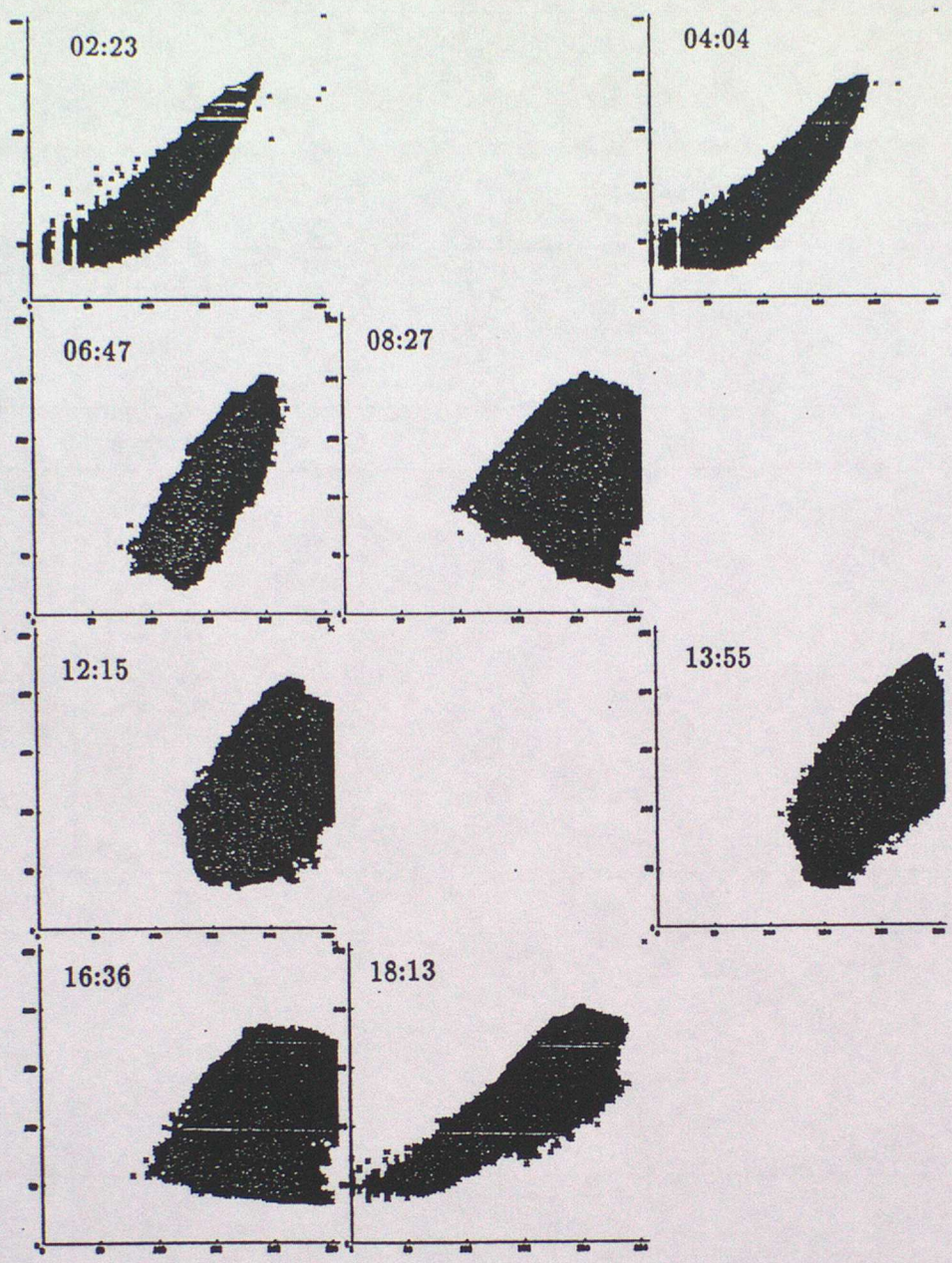

26. Example of single scatterplots T4 (*ordinate*) T3 (*abscissa*) for the images available on the 19/03/91 (GMT time). The limits of both the axis are $198 \div 308$ K.

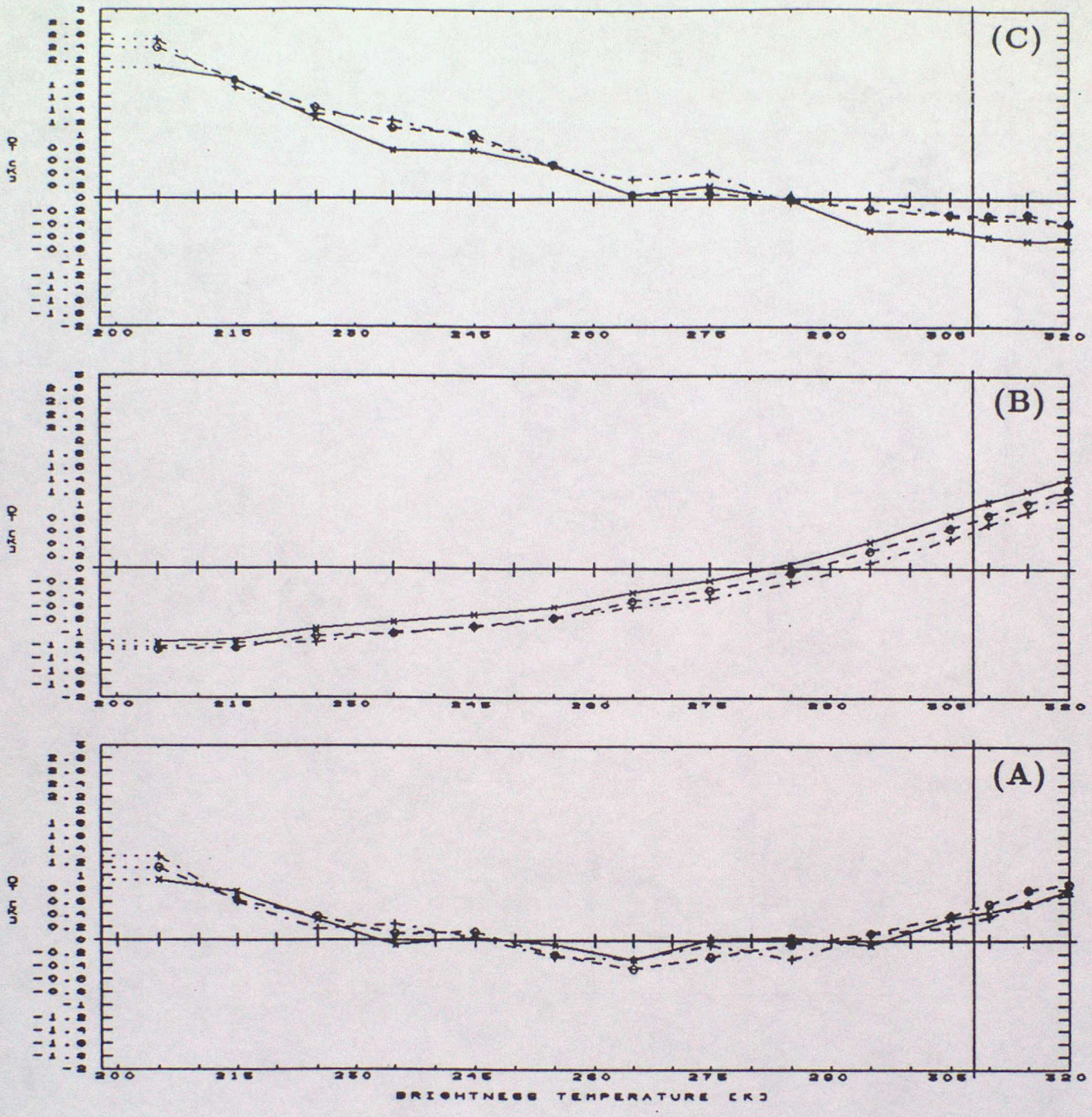

27. Correction factors (DT [K]) to be added to the GPCP-AIP/2 NOAA-11 data set:

A) T4; B) T5; C) T4-T5.

The limits of the ordinate are $-2.0 \div +3.0$ K. The curves relative to T4 have been computed assuming the same baseplate temperature for NOAA-10 as for NOAA-11. The correction for T4-T5 is approximate because of the hypothesis T5=T4 used for the computation of the correction factors (see text). Each curve is relative to an internal blackbody temperature ([——]: 282.35 K, [- - -]: 287.35 K, [-·-·-]: 292.15 K]).

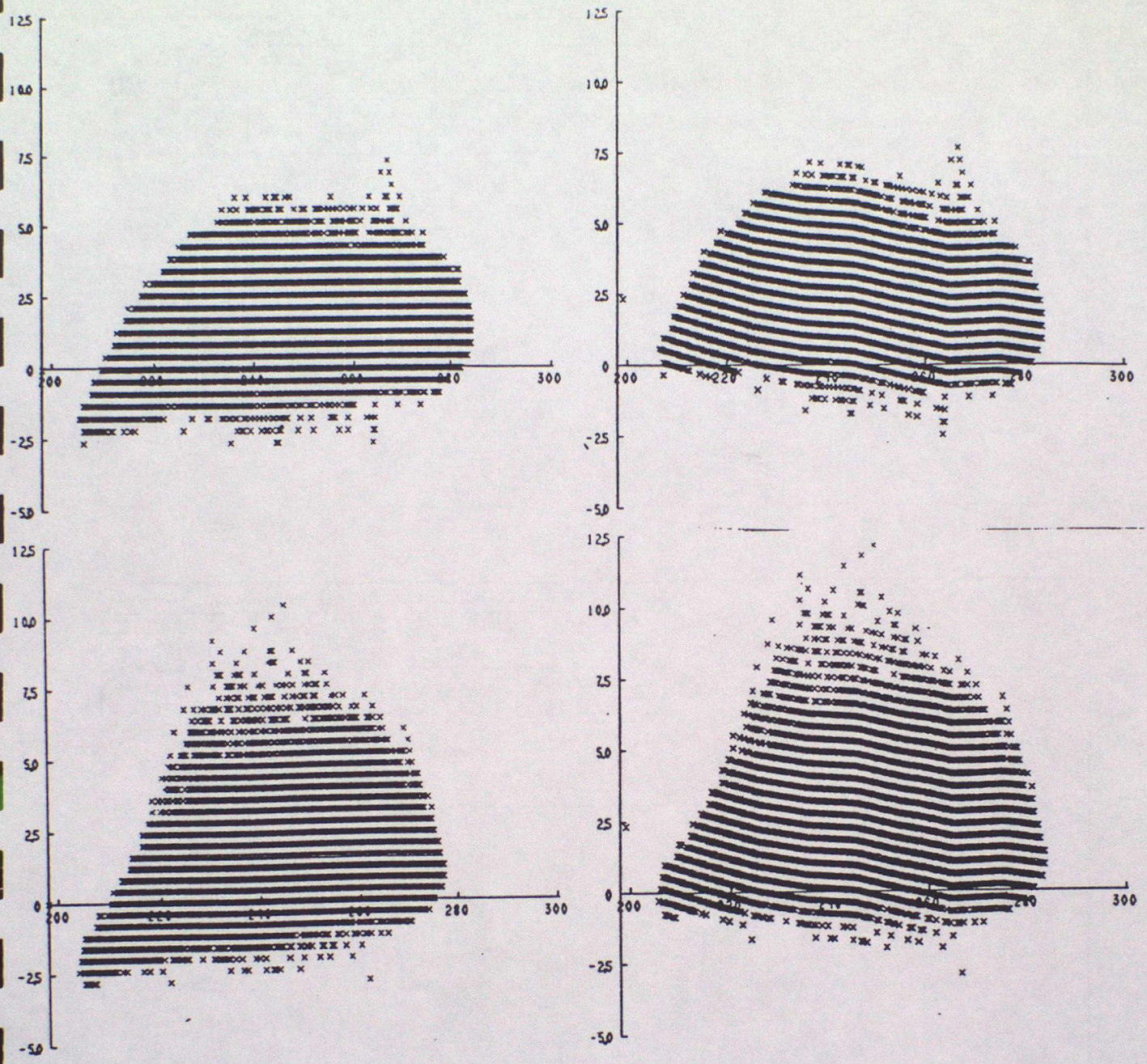

28. Example of single images scatterplots T4-T5 vs T4 for two of the GPCP-AIP/2 selected cases (91/03/08-02:46 (*lower panels*), 91/03/26-02:44 (*upper panels*)). The limits of the axis are $198 \div 300$ K for the abscissa and $-5 \div 12.5$ K for the ordinate. The scatterplots on the left have been plotted using uncorrected GPCP-AIP/2 data, the one on the right using the correction shown in Fig.27.

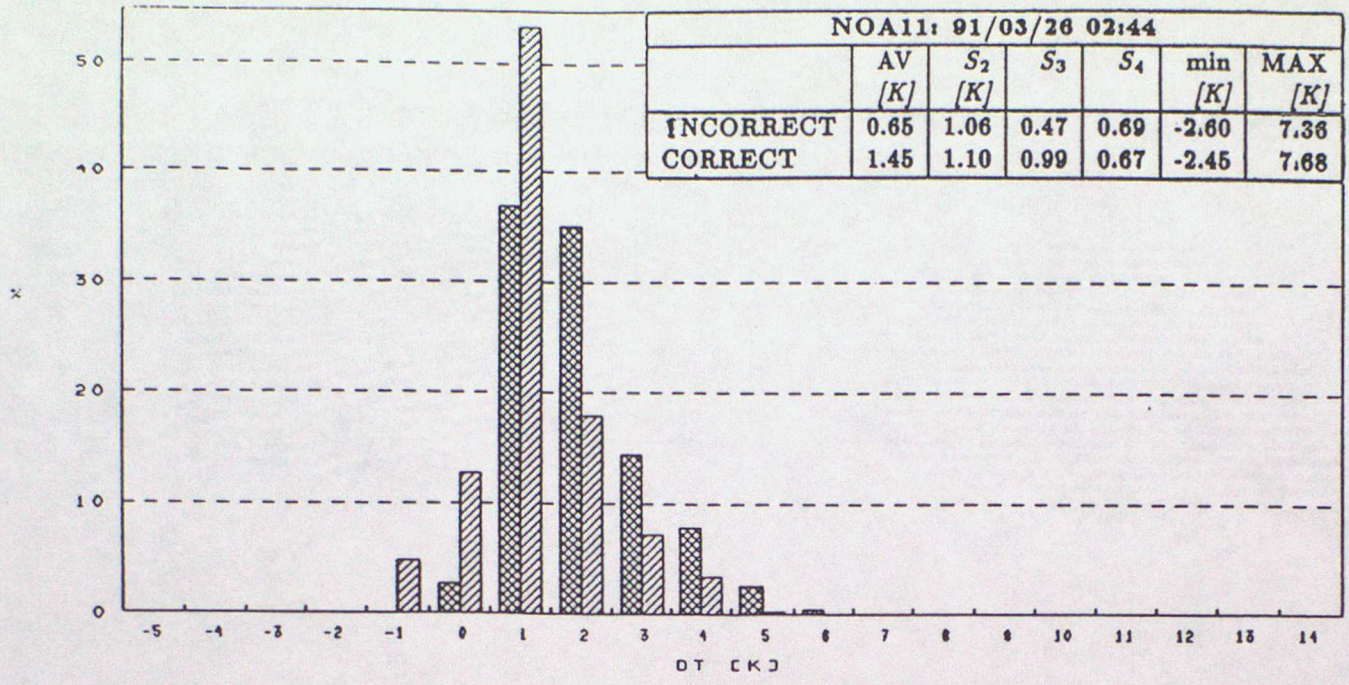

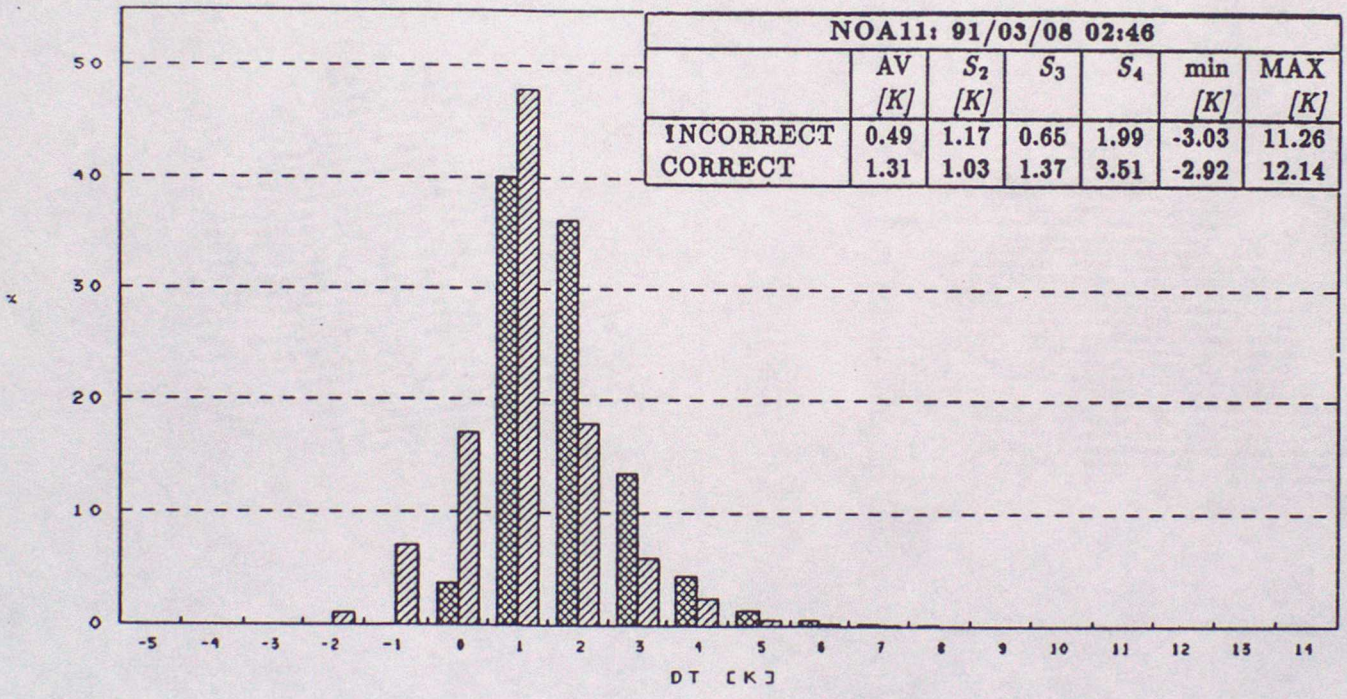

29. Example of statistics from T4-T5 images for two of the GPCP-AIP/2 selected cases (91/03/08-02:46 (*lower panel*), 91/03/26-02:44 (*upper panel*)). The histogram classes are 1 K wide and the value reported on the abscissa represent the upper limit (not included). The right bins ▨ are relative uncorrected GPCP-AIP/2 data, the left one ▩ are relative to the corrected image.

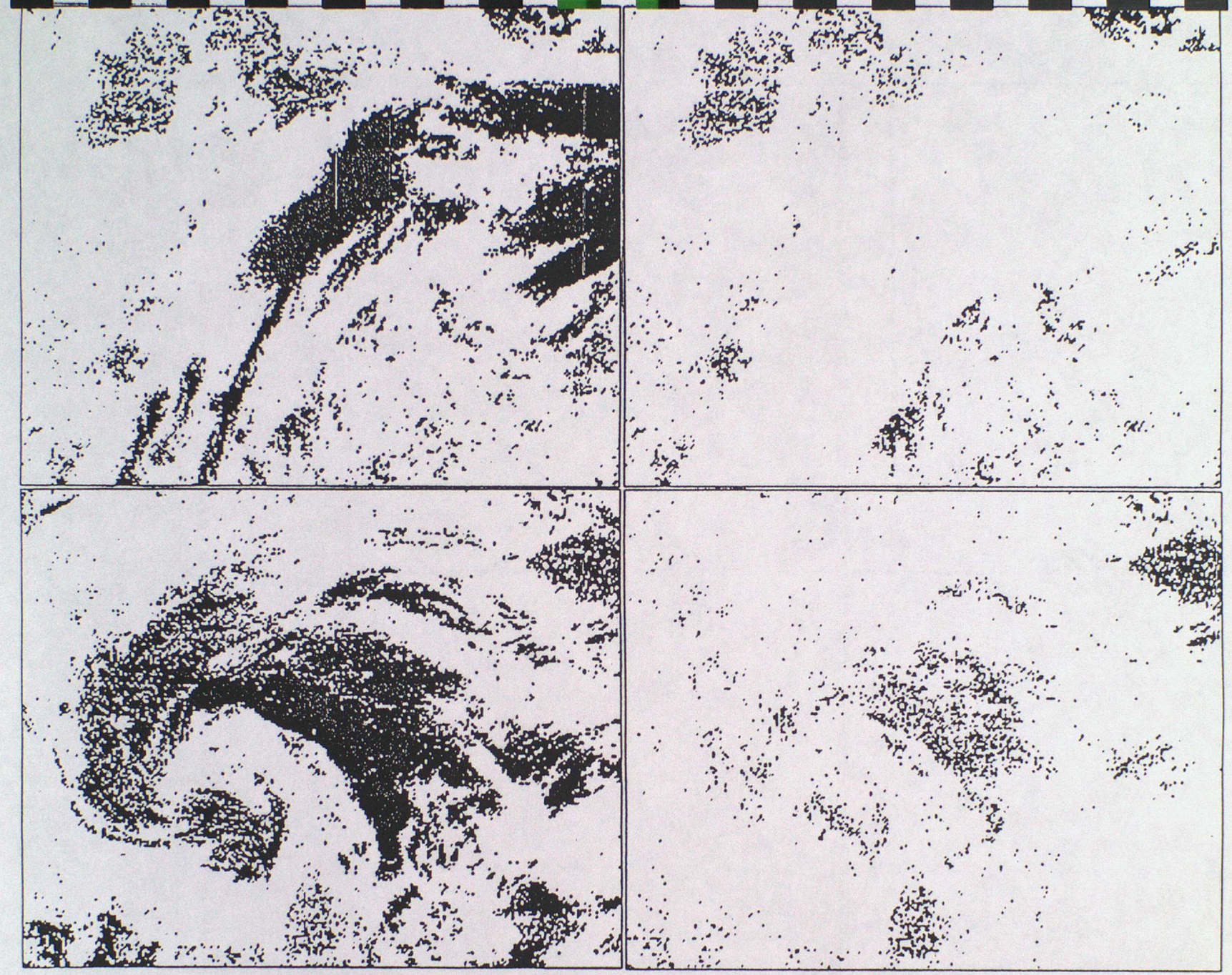

30. Example of 2-values images [black: $T4 < T5$, white: $T4 > T5$] for two of the GPCP-AIP/2 selected cases (91/03/08-02:46 (*lower panels*), 91/03/26-02:44 (*upper panels*)). For the images on the left uncorrected GPCP-AIP/2 data have been used, for the one on the right corrected (see text).

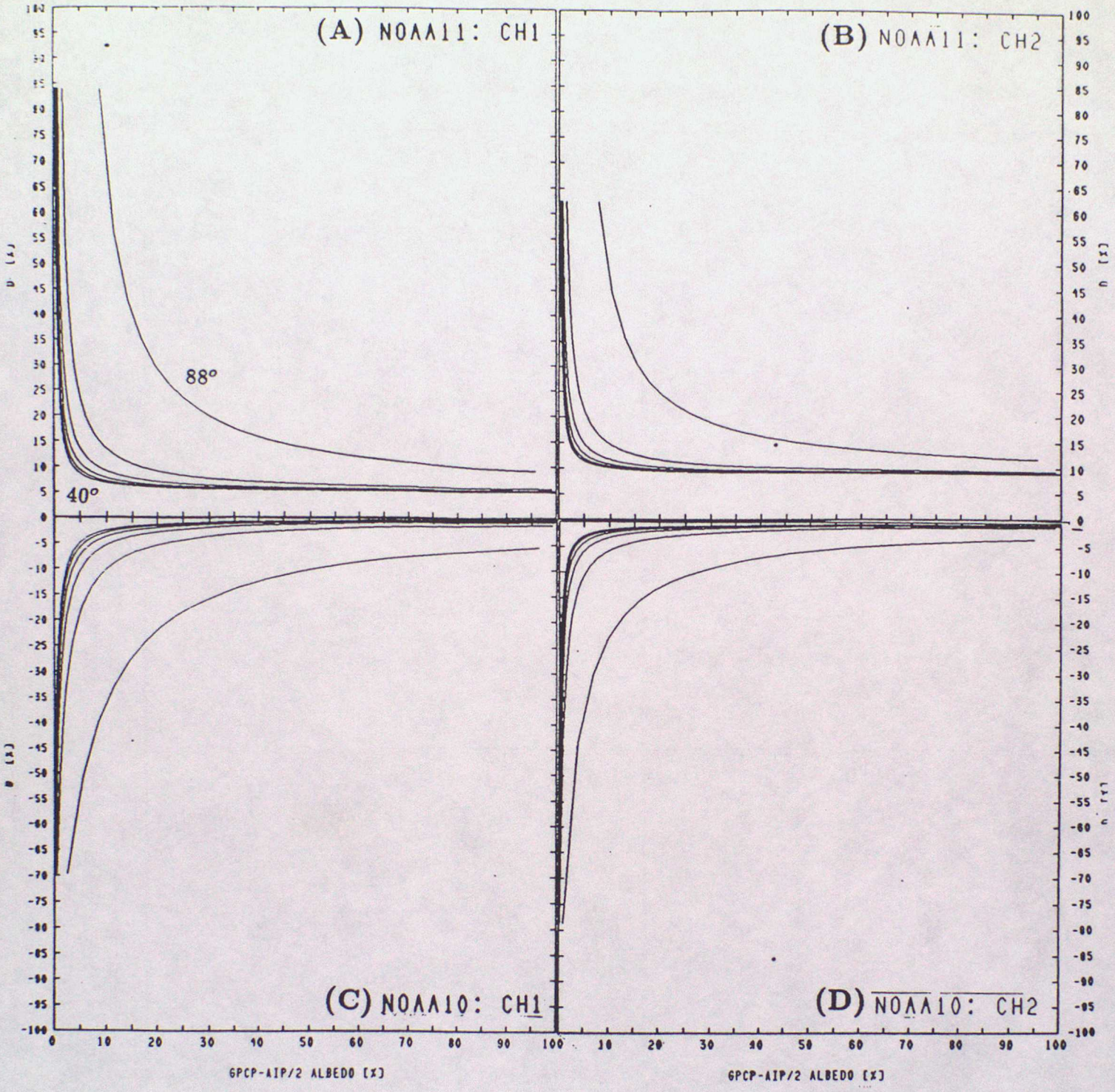

31. Percent difference ($D = 100. * (A_{Autosat2} - A_{NOAA})/A_{NOAA}$) between the albedo as computed for the GPCP-AIP/2 and the one obtained using the NOAA (Appendix B, Lauritson et al. 1988) calibration coefficients. The curves are computed for solar zenith angles of: 88°, 80°, 70°, 60°, 50° and 40° (beeing the 88° one the most external and the 40° the internal). Only values of $|D| < 100\%$ have been plotted.

A) NOAA-11 CH1 B) NOAA-11 CH2

C) NOAA-10 CH1 D) NOAA-10 CH2.